





# Disruption of a high-pressure unit during exhumation: Example of the Cycladic Blueschist unit (Thera, Ios and Naxos islands, Greece)

Alexandre Peillod<sup>1</sup>  | Clifford G. C. Patten<sup>1</sup> | Kirsten Drüppel<sup>2</sup> |  
Aratz Beranoaguirre<sup>1,3</sup>  | Armin Zeh<sup>2</sup> | Dominik Gudelius<sup>4</sup> |  
Simon Hector<sup>1</sup> | Jarosław Majka<sup>5,6</sup>  | Barbara I. Kleine-Marshall<sup>7</sup> |  
Andreas Karlson<sup>3</sup>  | Axel Gerdes<sup>8,9</sup> | Jochen Kolb<sup>1</sup>

<sup>1</sup>Chair of Geochemistry & Economic Geology, Karlsruhe Institute of Technology (KIT), Karlsruhe, Germany

<sup>2</sup>Department of Petrology, Karlsruhe Institute of Technology, Karlsruhe, Germany

<sup>3</sup>Department of Geosciences, Swedish Museum of Natural History, Stockholm, Sweden

<sup>4</sup>Department of Geosciences, Eberhard-Karls-Universität Tübingen, Tübingen, Germany

<sup>5</sup>Department of Earth Sciences, Mineralogy Petrology and Tectonics, Uppsala University, Uppsala, Sweden

<sup>6</sup>Department of Mineralogy, Petrography and Geochemistry, AGH University of Science and Technology, Krakow, Poland

<sup>7</sup>GeoZentrum Nordbayern, Friedrich-Alexander-Universität Erlangen-Nuremberg, Erlangen, Germany

<sup>8</sup>Frankfurt Isotope and Element Research Center (FIERCE), Goethe-Universität Frankfurt, Frankfurt am Main, Germany

<sup>9</sup>Institut für Geowissenschaften, Goethe-Universität Frankfurt, Frankfurt am Main, Germany

## Correspondence

Alexandre Peillod, Chair of Geochemistry & Economic Geology, Karlsruhe Institute of Technology (KIT), Karlsruhe, Germany.  
Email: alexandre.peillod@kit.edu

## Abstract

Reconstructing the original geometry of a high-pressure tectonic unit is challenging but important to understand the mechanisms of mountain building. While a single nappe is subducted and exhumed, nappe-internal thrusts may disrupt it into several subunits. The Middle-CBU nappe of the Cycladic Blueschist Unit (Hellenide subduction orogen, Greece) shows evidence of such disruption along a Trans-Cycladic-Thrust (TCT), however, the timing of this thrusting is unknown. Here, we report multi-petrological and geochronological data from the Middle-CBU nappe from the Thera and Ios islands (Greece). Using Zr-in-rutile thermometry coupled with quartz-in-garnet elastic barometry, average P–T and phase equilibrium thermodynamic modelling, we show that garnet growth in Ios occurred during prograde metamorphism at  $6.7 \pm 1.4$  kbar to  $13.0 \pm 1.6$  kbar and  $326 \pm 20^\circ\text{C}$  to  $506 \pm 13^\circ\text{C}$  ( $2\sigma$  uncertainty) followed by early exhumation to  $10.1 \pm 0.6$  kbar and  $484 \pm 14^\circ\text{C}$  and a greenschist facies overprint at  $5.7 \pm 1.2$  kbar and  $416 \pm 14^\circ\text{C}$ . For Thera, we constrain peak HP conditions of  $7.6 \pm 1.8$  kbar and  $331 \pm 18^\circ\text{C}$ , followed by exhumation and equilibration at  $\sim 2$  kbar and  $\sim 275^\circ\text{C}$  using average P–T and phase equilibrium thermodynamic modelling. For Ios, Uranium–Pb garnet geochronology provides ages of  $55.7 \pm 5.0$  Ma ( $2\sigma$  uncertainties) for prograde and  $40.1 \pm 1.4$  Ma for peak HP metamorphism. Combining our new P–T–t data from Thera and Ios islands with existing data from Naxos island, we conclude that the studied nappe segments represent remnants of a former coherent nappe. The P–T–t data define an Eocene subduction rate of  $2.1 \pm 1.0$  km/Ma, which is distinctly slower than the current subduction rate of 40–45 km/Ma. After subduction, the exhumation of the Middle-CBU nappe occurred during the Oligocene at different rates for different localities. The Middle-CBU nappe of Naxos was exhumed at a rate of  $\sim 6$  km/Ma, contrasting with the exhumation rate of  $\sim 3$  km/Ma calculated for

This is an open access article under the terms of the [Creative Commons Attribution-NonCommercial](https://creativecommons.org/licenses/by-nc/4.0/) License, which permits use, distribution and reproduction in any medium, provided the original work is properly cited and is not used for commercial purposes.

© 2023 The Authors. *Journal of Metamorphic Geology* published by John Wiley & Sons Ltd.

**Funding information**

Bolin Centre for Climate Research,  
Grant/Award Number:  
RA6\_19\_09\_Peillod; German Research  
Foundation, Grant/Award Numbers:  
INST121384/213-1, FUGG, 02020830221

Handling Editor: Dr. Sarah Penniston-  
Dorland

Ios. This result suggests that the Middle-CBU nappe of Naxos rocks was thrust on the Ios one during the Oligocene. Using P–T–t data and assuming realistic subduction angles during the Eocene and the Oligocene, we present a 2D structural reconstruction of the Middle-CBU nappe of these islands. This reconstruction helps to understand the mechanisms of subduction of a continental margin and its disruption during exhumation.

**KEYWORDS**

Cycladic Blueschist unit, Hellenides orogen, high-pressure metamorphism, thermobarometry methods, U–Pb garnet dating

**1 | INTRODUCTION**

Continental subduction leads to continental collision after which subduction either stops or steps outboard, allowing the accretion of a subsequent continental terrane (Ernst, 2001; van Hinsbergen et al., 2005). A nappe that has been subducted and experienced high-pressure (HP) metamorphism can be exhumed to a shallower crustal level through a series of different processes (Guillot et al., 2009; Platt, 1993 and reference therein). One of these

processes is wedge extrusion, which is thought to operate during exhumation of the Cycladic Blueschist Unit (CBU), Greece (Figure 1 – Aravadinou & Xypolias, 2017; Ducharme et al., 2022; Ernst et al., 1997; Gessner et al., 2001; Ring, Will, et al., 2007, Ring, Glodny, et al., 2007; Ring & Glodny, 2010 and references therein). A wedge extrusion may show internal deformation, which can cause the development of thrusts or thrust splays causing thickening of the lower parts of the wedge during exhumation. This can still lead to exhumation as long as normal

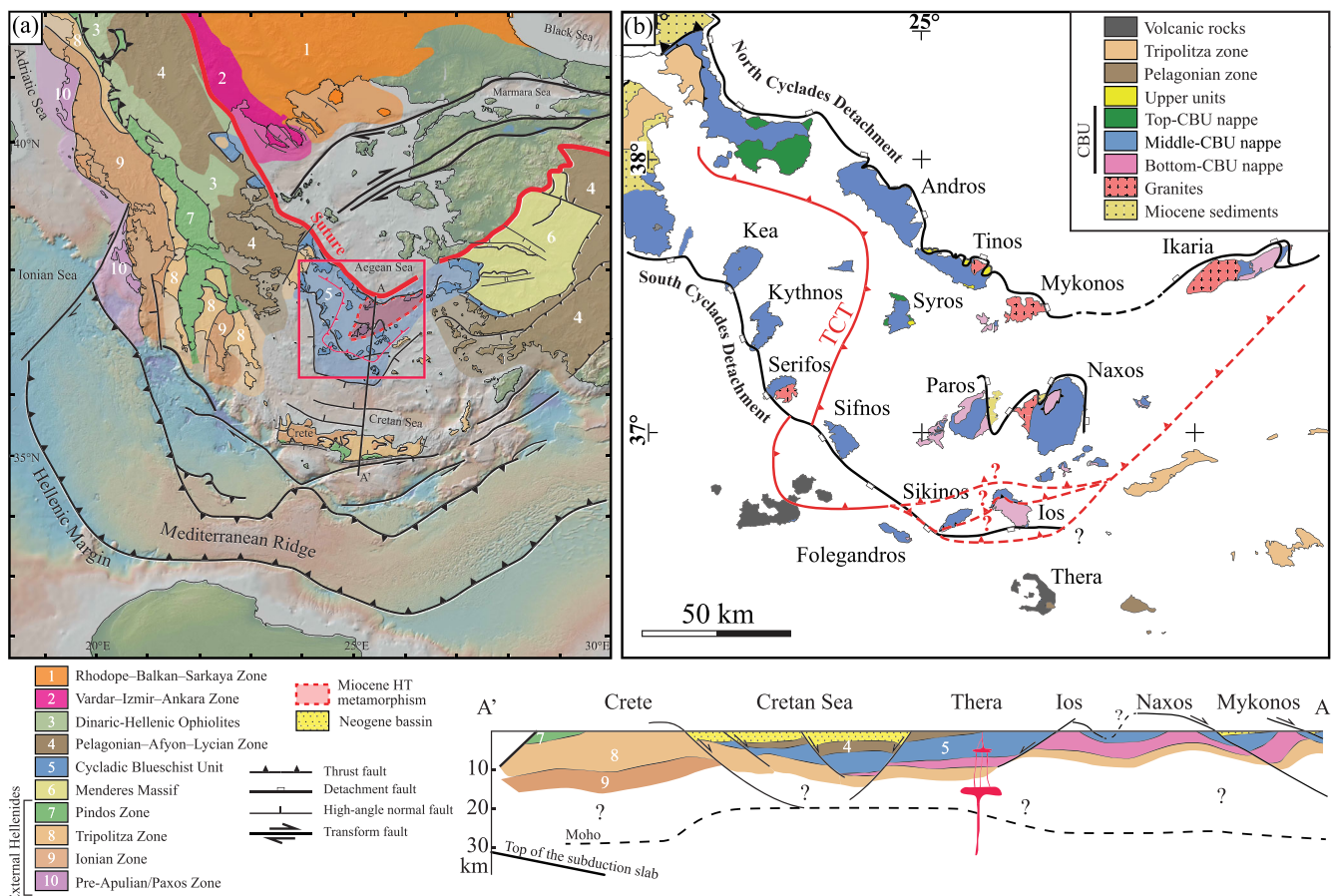


**FIGURE 1** (a) Simplified tectonic map of the Aegean Sea showing the major tectonic units (Dürr et al., 1978; Jolivet et al., 2021; Jolivet & Brun, 2010; Papanikolaou, 2013). Simplified N–S cross-section of the Cyclades (modified from Ring et al., 2003). (b) Tectonic map of the Cyclades. [Colour figure can be viewed at [wileyonlinelibrary.com](https://onlinelibrary.wiley.com)]

faulting at the top of the wedge is more dominant (Gerya et al., 2002; Grasemann et al., 2018; Peilod, Majka, et al., 2021; Ring & Glodny, 2021). The thrusts may disrupt coherent HP units. Detailed knowledge about the internal deformation and disruption of initially coherent HP nappes during exhumation is commonly lacking.

Recent research on the large-scale geometry of the CBU (Figure 1) defines three distinct and coherent HP nappes: the Bottom-, the Middle- and the Top-CBU nappes, which were successively accreted and exhumed in the Hellenic subduction zone between *c.* 55 and 30 Ma (Glodny & Ring, 2022). These nappes were exhumed as extrusion wedges (e.g. Ring, Glodny, et al., 2007), i.e., the base of each nappe unit represents a major thrust formed during HP metamorphism. Grasemann et al. (2018) show that these nappes were imbricated along the Trans Cycladic Thrust (TCT), which is a major thrust disrupting the CBU during its exhumation (Figure 1b). So far, the TCT mainly represents a 'tectonic concept', since it is largely mapped in between islands and used to explain the occurrence of high-P (~18–22 kbar) CBU rocks on the internal Cycladic islands (named Upper Cycladic Nappe) and lower-P (<12 kbar) CBU rocks on more external (southwestern) islands (named Lower Cycladic Nappe). Whether or not the TCT is exposed on some islands is a matter of debate. Ring and Glodny (2021) and Glodny and Ring (2022) propose that the thrust is exposed on Sikinos and possibly Ios island. Also debated is the exact timing of TCT activity. Grasemann et al. (2018) suggest that the TCT was active at *c.* 45 Ma during the subduction of the Middle-CBU nappe. However, their proposition does not account for the imbrication of <40 Ma HP nappes. Therefore, Glodny and Ring (2022) advocate an age of about 30 Ma for the TCT associated with the accretion of the Bottom-CBU nappe and exhumation of the Middle CBU nappe.

The Cycladic islands of Thera, Ios and Naxos are key areas for better understanding the role of the TCT because they expose the Bottom- and Middle-CBU nappes that apparently record different P–T–t conditions. However, the pressure–temperature–time (P–T–t) path of Ios and Thera remains poorly understood. Based on the available P–T data, the Middle-CBU nappe of Ios may either be in the hanging- (Huet, 2010) or footwall of the TCT (Grütter, 1993; Thomson et al., 2009; van der Maar & Jansen, 1983).

In this paper, we present new P–T–t data for the Middle-CBU nappe on Thera and Ios. Combining this new dataset with published data from Naxos allows us to reconstruct the structure of the Middle-CBU nappe and helps to better understand the development of the TCT during the Oligocene. Our new data provide a comprehensive overview of the architecture of the CBU and

improve the understanding of the mechanisms that may disrupt continental crust during its subduction and exhumation. Our results indicate that the Middle-CBU nappe behaved as a coherent unit during prograde metamorphism and experienced synchronous peak HP metamorphism in the Eocene. During Oligocene exhumation, internal deformation led to the development of thrust faults near the base of the nappe.

## 2 | GEOLOGICAL OVERVIEW

The Hellenides in the eastern Mediterranean form an arcuate orogen to the north of the active Hellenic margin (Figure 1a), which marks the NNE subduction of the African plate beneath Eurasia. The central Aegean in the Hellenides is a remarkable example of subduction-related burial and exhumation of a passive margin sequence followed by large-scale continental extension.

The Hellenides can be subdivided into continental units north and south of the oceanic Vardar–Izmir–Ankara Zone. To the north of this oceanic domain, the Rhodope–Balkan–Sarkaya Zone consists of Eurasian continental fragments, underneath which the oceanic crust of Neotethys was subducted during Jurassic and Cretaceous convergence (Jones & Robertson, 1991). The related suture is the ophiolitic Vardar–Izmir–Ankara Zone that experienced HP metamorphism during the late Cretaceous. The Dinaric–Hellenic Ophiolites can be interpreted as a SW margin of the Vardar–Izmir–Ankara Zone that got obducted onto the Adria continental margin (Schmid et al., 2020). To the south and below this oceanic domain follow the Pelagonian–Afyon–Lycian Zone, the CBU, the Menderes Massif and the External Hellenides, which comprise the Pindos Zone, the Tripolitza Zone, the Ionian Zone and the Pre-Apulian/Paxos Zone (Figure 1a – Avigad & Garfunkel, 1991; Dürr et al., 1978; Jones & Robertson, 1991; Ring et al., 1999; Ring & Layer, 2003; Schmid et al., 2020). The underlying Pelagonian–Afyon–Lycian Zone is a thrust belt, which largely escaped HP metamorphism with the exception of the Afyon unit that experienced Early Tertiary HP metamorphism (Kiliass et al., 2010; Schmid et al., 2020). To the south of the Pelagonian–Afyon–Lycian Zone, the remaining nappes, which comprise the CBU, consist of continental fragments of the Adriatic plate that experienced HP metamorphism during the Paleogene and Early Neogene.

The CBU is subdivided into three major, coherent nappes which are, in ascending structural order (Glodny & Ring, 2022): (1) the Bottom-CBU nappe consists of metasediments of the passive margin sequence and its (Cycladic) basement. The latter comprises Cambrian–Silurian garnet–mica schist and dolomitic

marble intruded by Carboniferous granites (Flansburg et al., 2019; van der Maar & Jansen, 1983; and references therein); (2) the Middle-CBU nappe comprises a Permo-Carboniferous to latest Cretaceous passive margin sequence composed of marble and metapelite, with minor quartzite and metabasite (Poulaki et al., 2019 and references therein) and (3) the Top-CBU nappe consists of ophiolitic rocks and garnet-mica schist embedded in a serpentinite chlorite-talc schist matrix (Okrusch & Bröcker, 1990 and references therein) and slices of the passive margin sequence.

The orogenic history of the CBU started in the early Cenozoic with subduction and HP metamorphism (e.g. Jolivet & Brun, 2010; Ring et al., 2010). The prograde subduction history is not well constrained. There are scarce data available on the P–T evolution and Sm–Nd and Lu–Hf garnet geochronology for the Middle- and the Top-CBU nappes, which indicate that some garnets grew quickly at near-peak P–T conditions, while other garnets grew slowly (e.g. Dragovic et al., 2015; Tual et al., 2022). For Sifnos Island, slowly growing garnets from the Middle-CBU nappe characterize a  $\sim 10$  Ma prograde P–T path from  $\sim 8$  kbar and  $\sim 300^\circ\text{C}$  at  $53.4 \pm 2.6$  Ma to  $20.6$ – $21.9$  kbar and  $490$ – $550^\circ\text{C}$  at  $45 \pm 0.5$  Ma (Dragovic et al., 2015). Additional P–T path data from Sifnos and Syros indicate near-isobaric heating from  $450$  to  $550^\circ\text{C}$  at high pressure of  $19$ – $22$  kbar at  $47$ – $43$  Ma (Dragovic et al., 2015; Gorce et al., 2021; Uunk et al., 2022) and  $53$ – $51$  Ma (Tual et al., 2022; Uunk et al., 2022) from different segments of the Middle- and Top-CBU nappes.

The Middle- and Top-CBU underwent peak metamorphism from *c.* 53 to 38 Ma, with older ages at the top of the nappe pile. Peak-metamorphic conditions range between  $\sim 8$  kbar and  $\sim 400^\circ\text{C}$  (e.g. Milos) and  $\sim 23$  kbar and  $\sim 600^\circ\text{C}$  (e.g. Syros), indicating that the nappes reached different depths during subduction. Remarkably, the Bottom-CBU nappe records distinctly lower-grade HP peak metamorphism (see reviews in Jolivet & Brun, 2010; Ring et al., 2010). The various stages of HP metamorphism in the Hellenic subduction zone may reflect stages of underthrusting and accretion, and subsequent exhumation of these nappes in extrusion wedges (Glodny & Ring, 2022; Kotowski et al., 2022; Uunk et al., 2022). Three distinct, lower-P metamorphic overprints are recorded for the different nappes and localities: (1) a greenschist facies overprint of the Top-CBU nappe of Samos, North Syros and western Turkey in the Eocene at *c.* 43–37 Ma (e.g. Kotowski et al., 2022; Lister & Forster, 2016; Ring, Will, et al., 2007), (2) a greenschist/lower-amphibolite facies equilibration of the Middle-CBU nappe of Naxos, South Syros and North Sifnos in the Oligocene at *c.* 33–27 Ma (Bröcker et al., 2013; Peillod et al., 2017; Peillod, Majka, et al., 2021; Skelton et al., 2019), and (3) a regional Miocene greenschist/

amphibolite facies metamorphic overprint affecting all three CBU nappes at 21–11 Ma (e.g. Beaudoin et al., 2015; Kumerics et al., 2005). This metamorphic overprint is associated with large-scale continental extension initiating at *c.* 23–21 Ma (Ring et al., 2010). This extension was mostly associated with greenschist facies metamorphism, but extension-related amphibolite facies rocks and migmatites are exposed in the central Cyclades (Buick & Holland, 1989; Jolivet et al., 2021 and references therein). Miocene–Pliocene syn-extensional sediments occur in the hanging wall of large-scale extensional detachments above the CBU (e.g. Kuhlemann et al., 2004).

### 3 | REVIEW OF DATA FROM NAXOS, IOS AND THERA ISLAND

#### 3.1 | Geology of Naxos

Naxos is located in the central Cyclades (Figure 1) and exposes the Bottom- and Middle-CBU nappes structurally below an Upper Unit made up of Miocene non-metamorphosed sedimentary and ophiolitic rocks (Buick, 1991; Glodny & Ring, 2022; Kuhlemann et al., 2004; Martin et al., 2006).

Two major structures are recognized (Figure 2a): (1) The Miocene top-to-the-NNE Naxos-Paros extensional fault system between the Upper Unit and the Middle-CBU nappe (Andriessen et al., 1979; Brichau et al., 2006; Cao et al., 2018; Gautier et al., 1993) and (2) the Carapace shear zone, a 500-m-thick shear zone straddling the Bottom/Middle-CBU nappe contact (Lister & Forster, 1996). The Carapace shear zone accommodated Oligocene thrusting of the Middle-CBU nappe onto the Bottom-CBU nappe (Peillod et al., 2017) and was subsequently reactivated during Miocene extensional deformation at amphibolite facies conditions (Lister & Forster, 1996; Vanderhaeghe, 2004). Extensional deformation controlled partial melting in the Bottom-CBU nappe, resulting in small leucogranite intrusions in the passive-margin sequence in the NW and in the granodiorite intrusion to the W (Jansen & Schuiling, 1976; and references therein). Partial melting drastically weakened the crust facilitating the large displacement of  $>80$  km along the Naxos–Paros extensional fault system (Ring et al., 2018).

##### 3.1.1 | Bottom-CBU nappe

There is no evidence of an HP event affecting the migmatitic Cycladic basement of the Bottom-CBU nappe (Vanderhaeghe et al., 2018). From metapelitic rafts within the migmatite, initial P–T conditions of  $8.0$ – $9.7 \pm 2$  kbar

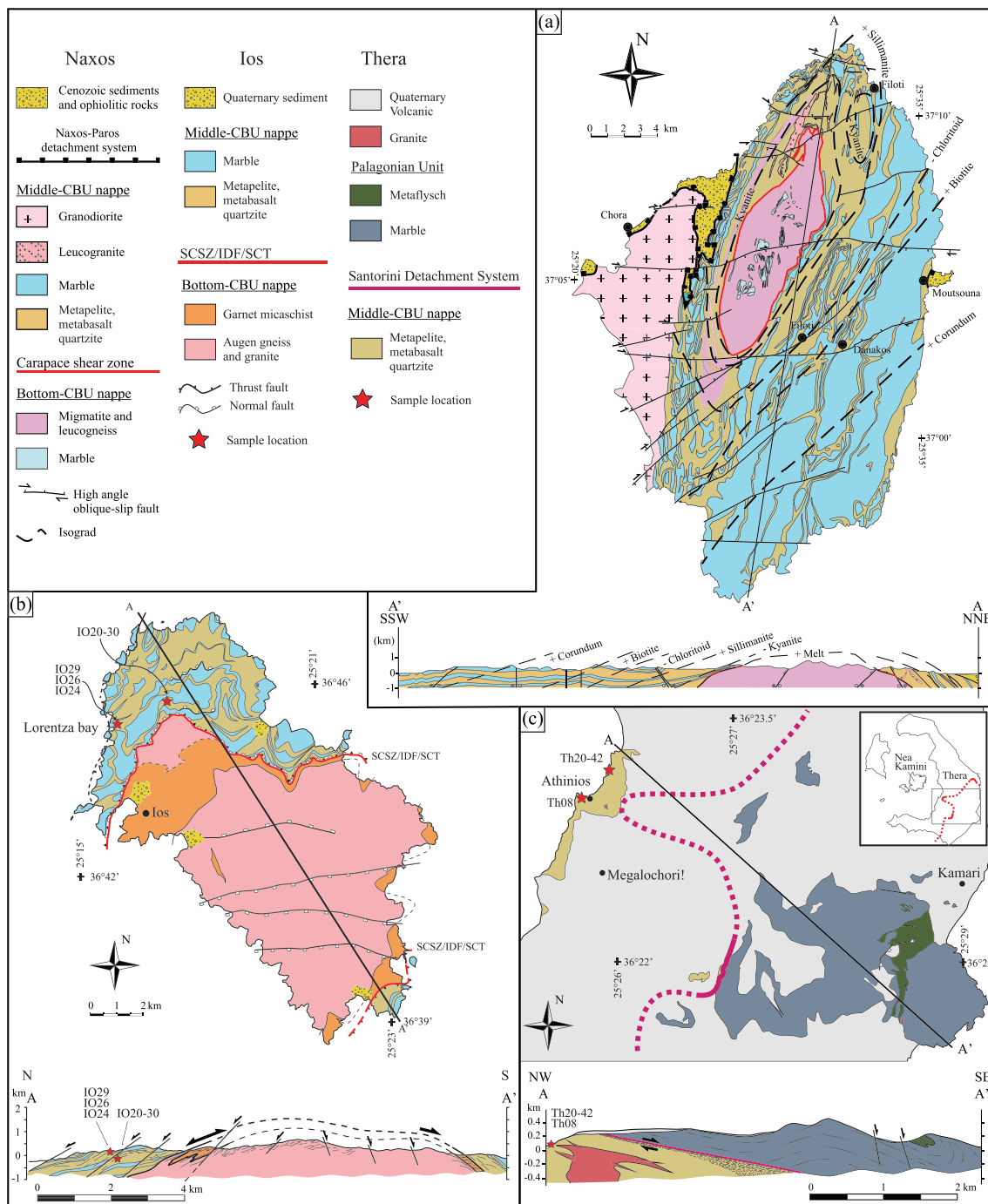


**FIGURE 2** (a) Geological map and cross-section of Naxos (modified from Jansen & Schuling, 1976; Kruckenberg et al., 2010; Lamont et al., 2019; Vanderhaeghe, 2004). (b) Geological map and cross-section of Ios (modified from Huet et al., 2009; Thomson et al., 2009; Forster & Lister, 1999b) with sample locations. (c) Geological map and cross-section of Thera showing the pre-volcanic basement (modified from Schneider et al., 2018) with sample locations. Coordinates are given in degree minute decimal (WGS84). [Colour figure can be viewed at [wileyonlinelibrary.com](https://onlinelibrary.wiley.com)]

and  $600 \pm 50^\circ\text{C}$  are calculated, followed by  $6.0\text{--}8.0 \pm 2.5$  kbar and  $670 \pm 50^\circ\text{C}$  (Buick & Holland, 1989) using average P-T (avP-T) and garnet-biotite thermometry (Figure 3). Post-peak metamorphism was estimated at  $4\text{--}6$  kbar and  $600\text{--}650^\circ\text{C}$  using TWEEQU (Duchêne et al., 2006; Martin, 2004). From a migmatite sample,

Lamont et al. (2019) estimated a prograde path from  $6.0\text{--}6.5$  kbar at  $550\text{--}590^\circ\text{C}$ , to  $\sim 9.5$  kbar at  $\sim 700^\circ\text{C}$  and subsequent near-isothermal decompression to  $\sim 6.5$  kbar and  $710\text{--}720^\circ\text{C}$ , then finally  $\sim 4.9$  kbar and  $\sim 705^\circ\text{C}$  using garnet isopleths calculated with the Thermocalc software (Figure 3).



U–Pb zircon ages of  $20.7 \pm 1.0$  Ma and  $17.4 \pm 0.6$  Ma were interpreted to constrain partial melting (Keay et al., 2001). A slightly wider age range from  $24.2 \pm 0.7$  Ma to  $16.6 \pm 0.3$  Ma is reported using in-situ (SIMS) U–Pb zircon dating (Vanderhaeghe et al., 2018). Based on  $^{40}\text{Ar}/^{39}\text{Ar}$  white mica and hornblende dating, peak HT metamorphism occurred between 19.8 and 15 Ma (Wijbrans & McDougall, 1988). The authors suggest that peak HT metamorphism more likely occurred close to 15 Ma. This age correlates well with U–Pb ages of zircon rims in amphibolite of the lower passive-margin sequence, indicating that conditions conducive to zircon growth during HT have persisted at least until 15–14 Ma (Bolhar et al., 2017). Rb–Sr multi-mineral ages reported for pegmatite and migmatite show that HT metamorphic conditions and partial anatexis during top-to-the-NNE extensional shearing in the Carapace shear zone lasted until about 14–12 Ma (Ring et al., 2018). U–Pb zircon dating yielded ages between 15.4 and 11.3 Ma for S-type leuco- and biotite-granites and 13.2 to 12.3 Ma for the I-type granodiorite in western Naxos (Bolhar et al., 2017; Keay et al., 2001).

### 3.1.2 | Middle-CBU nappe

A synthesis of the petrological and geochronological studies of the Middle-CBU nappe in Naxos reveals four metamorphic stages (1) HP metamorphism comprising prograde and peak HP metamorphism; (2) initial exhumation; and (3) an HT overprint followed by (4) final exhumation. The lower and upper parts of the Middle-CBU nappe on Naxos are differently affected by these metamorphic stages.

#### *Lower parts of the Middle-CBU nappe.*

The original HP metamorphic assemblages are mostly obscured by the subsequent HT overprint and are only preserved in garnet cores. Martin (2004) estimates conditions of 15–20 kbar and 500–600°C for peak HP metamorphism of metapelite rocks of the lower parts of the Middle-CBU nappe using garnet isopleths with Theriak/Domino software (Figure 3). In line with this, Peillod, Majka, et al. (2021) calculate prograde to peak HP metamorphism at  $15.4 \pm 0.8$  kbar to  $19.9 \pm 0.6$  kbar and at  $496 \pm 16^\circ\text{C}$  to  $572 \pm 7^\circ\text{C}$  for garnet-biotite schist, using garnet isopleths from the Theriak/Domino software and from combined quartz-in-garnet (QuiG) and Zr-in-rutile thermobarometry (Figure 3). The HP stage is followed by near-isothermal decompression to  $\sim 10$  kbar and subsequent near-isobaric heating from 500–550 to 600–650°C (Martin, 2004; Peillod, Majka, et al., 2021). At the structurally lowest levels of the Middle-CBU nappe peak T is estimated at 670–700°C at 8–10 kbar (Figure 3 – Duchêne

et al., 2006; Lamont et al., 2019), garnet isopleths from the Theriak/Domino, avP–T and TQW software, Ti-in-biotite thermometry and various thermodynamic reactions like garnet-biotite thermometry.

Two different models are proposed to be responsible for the high-T metamorphism: (1) Based on structural data and isopleths calculated for core-to-rim compositions of garnet in assemblage with amphibole, Lamont et al. (2019) suggest that the HT event is caused by a subsequent Barrovian-type metamorphic event, with prograde P–T conditions increasing from  $\sim 6.1$  kbar and 600°C to  $\sim 10$  kbar and  $\sim 670^\circ\text{C}$ . The authors moreover claim that the lowermost part of the Middle-CBU sequence did not experience HP metamorphism at all and consequently conclude that it represents a different tectonic unit, termed Koronos unit, that is separated from the upper part of the sequence by the Eocene/Oligocene Zas shear zone. (2) In contrast, Peillod, Tehler, and Ring (2021) propose that HT metamorphism was caused by near-isobaric heating at  $\sim 10$  kbar, following a first decompression after HP metamorphism. A detailed structural investigation of the Zas shear zone by Peillod, Tehler, and Ring (2021) reveals no significant localization of deformation. Instead, Peillod, Tehler, and Ring (2021) show that deformation can be attributed to Miocene greenschist top-to-the-NNE extensional shearing with no evidence of a pre-Miocene deformation event. Remarkably, exceptional metabauxite deposits are exposed within the entire Naxos Middle-CBU nappe, indicating that the Middle-CBU nappe represents one single tectonic unit (Peillod, Tehler, & Ring, 2021). Consistent with this interpretation,  $\text{Fe}^{3+}$ -rich kyanite in the metabauxite is suggested to be a relic of HP metamorphism (Feenstra, 1985). Likewise, Duchêne et al. (2006) and Martin et al. (2006) interpret the chemical compositions and  $\delta^{18}\text{O}$  isotope data of garnet cores and the subsequently grown garnet rims as well as the LREE-rich composition of epidote within the so-called Koronos unit in terms of HP metamorphism. Following these arguments and P–T data presented by Peillod, Majka, et al. (2021) and Martin (2004), the entire Middle-CBU nappe of Naxos, including the lowermost part, initially underwent HP metamorphism, despite the absence of clear HP index minerals (e.g., glaucophane, lawsonite and omphacite).

The heating stage is followed by late decompression to 3–6 kbar and  $\sim 600^\circ\text{C}$  using avP–T (Buick & Holland, 1989; Duchêne et al., 2006; Lamont et al., 2019; Peillod, 2018), thermodynamic models (Lamont et al., 2019; Peillod, Majka, et al., 2021) and “classical” thermobarometry (Figure 3 – Duchêne et al., 2006; Lamont et al., 2019).

Two episodes of zircon growth in one metamorphic zircon rim (“A” rim of Martin et al., 2006 – Figure 3) date HP

metamorphism at 61–48 Ma and 47–41 Ma in the lower Middle-CBU nappe. The youngest age group is confirmed by U–Pb zircon ages 47–38 Ma with a weighted mean of  $39.6 \pm 1.1$  Ma (Bolhar et al., 2017). These authors propose that the older >60 Ma rim may result from mixed analysis of zircon rim and cores. Rb–Sr and  $^{40}\text{Ar}/^{39}\text{Ar}$  ages of 38–35 Ma date exhumation soon after the peak HP metamorphism at c. 40 Ma (Cao et al., 2018; Peillod et al., 2017; Villa et al., 2022). In contrast, Lamont et al. (2023) report two U–(Th)–Pb allanite ages at  $50 \pm 5$  and  $49.4 \pm 5$  Ma interpreted to date peak HP metamorphism (Figure 3). However, according to their petrographic observations and thermodynamic model allanite might have already formed during prograde metamorphism. Therefore, their ages likely date prograde allanite formation and are thus difficult to interpret without additional observations. The lowermost Middle-CBU Nappe was near-isothermally exhumed to mid-crustal, lower amphibolite facies levels ( $\sim 10$  kbar) at  $29.3 \pm 1.3$  Ma in the (Figure 3 – Duchêne et al., 2006).

Following initial exhumation, the HT event started between  $23.1 \pm 1.0$  and  $19.8 \pm 0.2$  Ma based on  $^{40}\text{Ar}/^{39}\text{Ar}$  hornblende plateau ages (Figure 3 – Wijbrans & McDougall, 1988). These authors suggest that the HT metamorphism lasted until  $15.0 \pm 0.2$  Ma followed by cooling until c. 11 Ma based on  $^{40}\text{Ar}/^{39}\text{Ar}$  hornblende, muscovite and biotite plateau ages. Other  $^{40}\text{Ar}/^{39}\text{Ar}$  age data, as well as multi-mineral Rb–Sr and U–Pb zircon age data, yield similar results (Bolhar et al., 2017; Cao et al., 2017; Cao et al., 2018; Duchêne et al., 2006; Martin et al., 2006; Ring et al., 2018). Cao et al. (2017) report  $^{40}\text{Ar}/^{39}\text{Ar}$  white mica ages of  $12.6 \pm 0.6$  Ma from the Moutsouna detachment shear zone at the eastern boundary of the metamorphic core complex and of  $10.4 \pm 0.9$  Ma to  $8.4 \pm 1.5$  Ma for ductile deformation along the Naxos extensional shear zone in northern Naxos (Figure 3). Mancktelow et al. (2016) report a K–Ar age of  $9.7 \pm 1$  Ma for a fault gouge from the Naxos detachment.

#### *Upper parts of the Middle-CBU nappe.*

For the upper part of the Middle-CBU nappe, mineral assemblages in HP rocks indicate that prograde replacement of lawsonite by epidote and paragonite occurred simultaneously with the growth of garnet that hosts these pseudomorphs as inclusions (Avigad, 1998; Peillod et al., 2017). For this assemblage prograde P–T conditions were calculated at  $12.8 \pm 0.5$  kbar and  $457 \pm 12^\circ\text{C}$ , using the avP–T routine (avP–T) of the Thermocalc software (Peillod et al., 2017). Peak HP conditions were initially calculated at >12 kbar and  $470 \pm 50^\circ\text{C}$  using thermodynamic reactions (Avigad, 1998) and re-estimated at  $15.9 \pm 0.7$  kbar and  $597 \pm 22^\circ\text{C}$  using avP–T (Figure 3 – Peillod et al., 2017). Post-peak HP metamorphism occurred at 8–15 kbar and  $400\text{--}540^\circ\text{C}$  (Lamont et al., 2019).

Thermodynamic reactions and avP–T constrain a subsequent greenschist facies equilibration stage at  $3.8 \pm 1.1$  kbar and  $385 \pm 35^\circ\text{C}$  (Avigad, 1998; Peillod et al., 2017).

Rb–Sr multi-mineral dating provides ages of  $40.5 \pm 1.0$  and  $38.3 \pm 0.5$  Ma for peak HP metamorphism (Figure 3 – Peillod et al., 2017). These ages are in line with Rb–Sr whole-rock and white-mica ages of c. 42 Ma for pristine HP rocks (Andriessen et al., 1979). A U–(Th)–Pb allanite age of  $40.5 \pm 2.7$  Ma (Lamont et al., 2023) is interpreted to date post-peak HP metamorphism (Figure 3), however, this age is difficult to interpret (see discussion above). Additionally, K–Ar and  $^{40}\text{Ar}/^{39}\text{Ar}$  white-mica ages for HP metamorphism show a large age spread of 60–40 Ma with a cluster at c. 45–40 Ma (Figure 3 – Andriessen, 1978; Andriessen et al., 1979; Cao et al., 2018; Villa et al., 2022; Wijbrans & McDougall, 1988, Wijbrans & McDougall, 1986). This large spread has been attributed to an excess  $^{40}\text{Ar}$  (Andriessen et al., 1979). Given the widespread problem of excess  $^{40}\text{Ar}$  in HP white mica, the youngest K–Ar and  $^{40}\text{Ar}/^{39}\text{Ar}$  white-mica ages usually represent a good approximation of the true age of peak HP metamorphism (Ring et al., 2020; Warren et al., 2012). Additionally, Wijbrans and McDougall (1988) prove strong disequilibrium in white mica as expressed by upward convex age spectra and propose that these spectra result from the mixing of early HP phengite and texturally late muscovite. Similar observations indicating significant disequilibrium due to either excess  $^{40}\text{Ar}$  or mixing of different white-mica populations (i.e. prograde, peak HP and retrograde) were also reported by Cao et al. (2018).

In the Oligocene at  $32 \pm 3$  Ma, the upper parts of the Middle-CBU nappe were affected by a first retrograde greenschist facies overprint (multi-mineral Rb–Sr (Peillod et al., 2017) and U–(Th)–Pb xenotime geochronology (Lamont et al., 2023 – Figure 3). Zircon fission-track (ZFT) ages of  $25.2 \pm 3.8$  and  $20.5 \pm 2.4$  Ma constrain cooling through  $\sim 240^\circ\text{C}$  (Seward et al., 2009), which indicates that the uppermost Middle-CBU Nappe reached the brittle crust before the Miocene HT event commenced lower down in the nappe pile. Cao et al. (2018, 2017) suggest that localized greenschist facies re-equilibration occurred in small-scale shear zones at  $\sim 25\text{--}15$  Ma in deeper parts of the Naxos CBU nappes (Figure 3). ZFT ages indicate progressive cooling from  $25.2 \pm 3.8$  Ma in the upper part of the sequence to  $9.3 \pm 2.8$  Ma towards the lower part of the sequence (Seward et al., 2009).

## 3.2 | Ios island

Ios consists of a domal architecture characteristic of a metamorphic core complex (Figure 2b – van der Maar &



Jansen, 1983). The Middle-CBU nappe is composed of schist, marble and metavolcanic rocks variably metamorphosed at blueschist, eclogite and greenschist facies conditions (van der Maar & Jansen, 1983). Locally, eclogite lenses are preserved (Forster & Lister, 1999a). Small syn-subduction thrusts imbricate the sedimentary sequence (Poulaki et al., 2019). The Bottom-CBU nappe mainly comprises garnet-mica schist into which variably deformed Carboniferous orthogneiss intruded. The contact between the Middle- and the Bottom-CBU nappes indicate different episodes of contractional and extensional deformation either interpreted as (1) an Eocene–Oligocene top-to-the-south extensional shear zone (the South Cyclades Shear Zone — SCSZ), truncated by the Miocene, south-dipping Ios detachment fault (IDF) (Baldwin & Lister, 1998; Forster et al., 2020; Forster & Lister, 1999b; Mizera & Behrmann, 2016) or (2) an Eocene/Oligocene subduction-related top-to-the-south thrust fault, the South Cyclades Thrust (SCT) (Huet et al., 2009; Thomson et al., 2009; van der Maar & Jansen, 1983) that was later reactivated during Miocene exhumation as either a single top-to-the-north, low-angle normal fault (Jolivet et al., 2010) or bivergent normal faults (Mizera & Behrmann, 2016; Thomson et al., 2009; Vandenberg & Lister, 1996). The latter interpretation is supported by structural evidence and the gap in peak pressures between the Middle- and the Bottom-CBU nappe on the nearby island of Sikinos (Ring & Glodny, 2021). Detrital zircon provenance data indicate a continuous stratigraphic record and provenance evolution from the Bottom-CBU nappe into the Middle-CBU nappe (Flansburg et al., 2019; Poulaki et al., 2019; Poulaki et al., 2021).

### 3.2.1 | Bottom-CBU nappe

Rare glaucophane, garnet, chloritoid, clinozoisite, chlorite, white mica and rutile indicate that the bottom nappe experienced HP metamorphism (Grütter, 1993). The absence of clinopyroxene (jadeite or omphacite) suggests moderate HP conditions. Based on observed mineral assemblages, peak P–T conditions of ~9–11 kbar and 350–500°C followed by exhumation to 5–7 kbar and 350–420°C were determined by mineral reactions and avP–T calculation (Figure 4 – Grütter, 1993; Thomson et al., 2009; van der Maar & Jansen, 1983). These results contrast with the P–T data of Huet (2010), who propose prograde and peak P–T conditions from  $13.0 \pm 1.3$  kbar and  $460 \pm 20^\circ\text{C}$  to  $15.5\text{--}16.5 \pm 1.3$  kbar and  $500\text{--}550 \pm 20^\circ\text{C}$  in the stability field of garnet, epidote, chlorite and white mica, followed by exhumation to  $8 \pm 2$  kbar and  $420 \pm 20^\circ\text{C}$  in the stability field of garnet, albite and white mica.

There is also no consensus on the age of HP metamorphism.  $^{40}\text{Ar}/^{39}\text{Ar}$ , K–Ar white mica and U–Pb zircon dating yield late Cretaceous to Eocene ages (Baldwin & Lister, 1998; Flansburg et al., 2019; Forster et al., 2020; Forster & Lister, 2009; Henjes-Kunst & Kreuzer, 1982; Poulaki et al., 2021). Most of the  $^{40}\text{Ar}/^{39}\text{Ar}$  spectra show a distinct staircase pattern making interpretations difficult. Eocene metamorphic zircon ages (65–40 Ma) are rare and have no relationships with the HP parageneses (Poulaki et al., 2021).

A single, well-defined  $^{40}\text{Ar}/^{39}\text{Ar}$  plateau age of  $20.6 \pm 0.2$  Ma is interpreted to date the greenschist facies overprint (Baldwin & Lister, 1998). These authors also report an age of  $31.9 \pm 0.2$  Ma but do not interpret it.  $^{40}\text{Ar}/^{39}\text{Ar}$  ages on white mica and K-feldspar show that the SCSZ may have initiated at c. 35 Ma as a top-to-the-south shear zone and was overprinted with top-to-the-north shear sense at c. 25 Ma (Forster & Lister, 2009). Additionally, Forster et al. (2020) suggest that these two episodes are characterized by rapid cooling from ~500°C to ~400°C and from 400°C to <200°C based on  $^{40}\text{Ar}/^{39}\text{Ar}$  K-feldspar data. Similar ages are obtained from Rb–Sr and U–Pb geochronology (Poulaki et al., 2021; Thomson et al., 2009).

Exhumation to shallow crustal levels and cooling to <200°C between 15 and 7 Ma (U–Th)/He zircon and apatite and AFT ages) show that the Bottom- and Middle-CBU nappes were exhumed as a coherent block after c. 15 Ma (Flansburg et al., 2022; Hejl et al., 2003, 2008; Thomson et al., 2009).

### 3.2.2 | Middle-CBU nappe

A synthesis of the petrological and geochronological studies of the Middle-CBU nappe Ios reveals at least four Cenozoic metamorphic stages: (1) prograde; (2) peak HP; (3) early/first exhumation; and (4) final/second exhumation (Figure 4). The P–T estimates for the prograde and peak HP metamorphism vary widely depending on the methods applied.

The prograde metamorphic evolution is determined from the transition of lawsonite blueschist to epidote blueschist facies mineral assemblages and estimated at ~8.8 kbar and 330°C to 12.6 kbar and 475°C using avP–T (Grütter, 1993). Similar peak HP conditions are calculated for these rocks using avP–T and thermodynamic reactions (Thomson et al., 2009; van der Maar & Jansen, 1983). In contrast, P–T phase diagrams calculated with the Theriak-Domino software for similar rocks yield ~6 kbar higher prograde to peak P values ranging from ~16 kbar and 490°C to 18.5 kbar and 510°C (Huet, 2010). P–T conditions of an early exhumation stage are

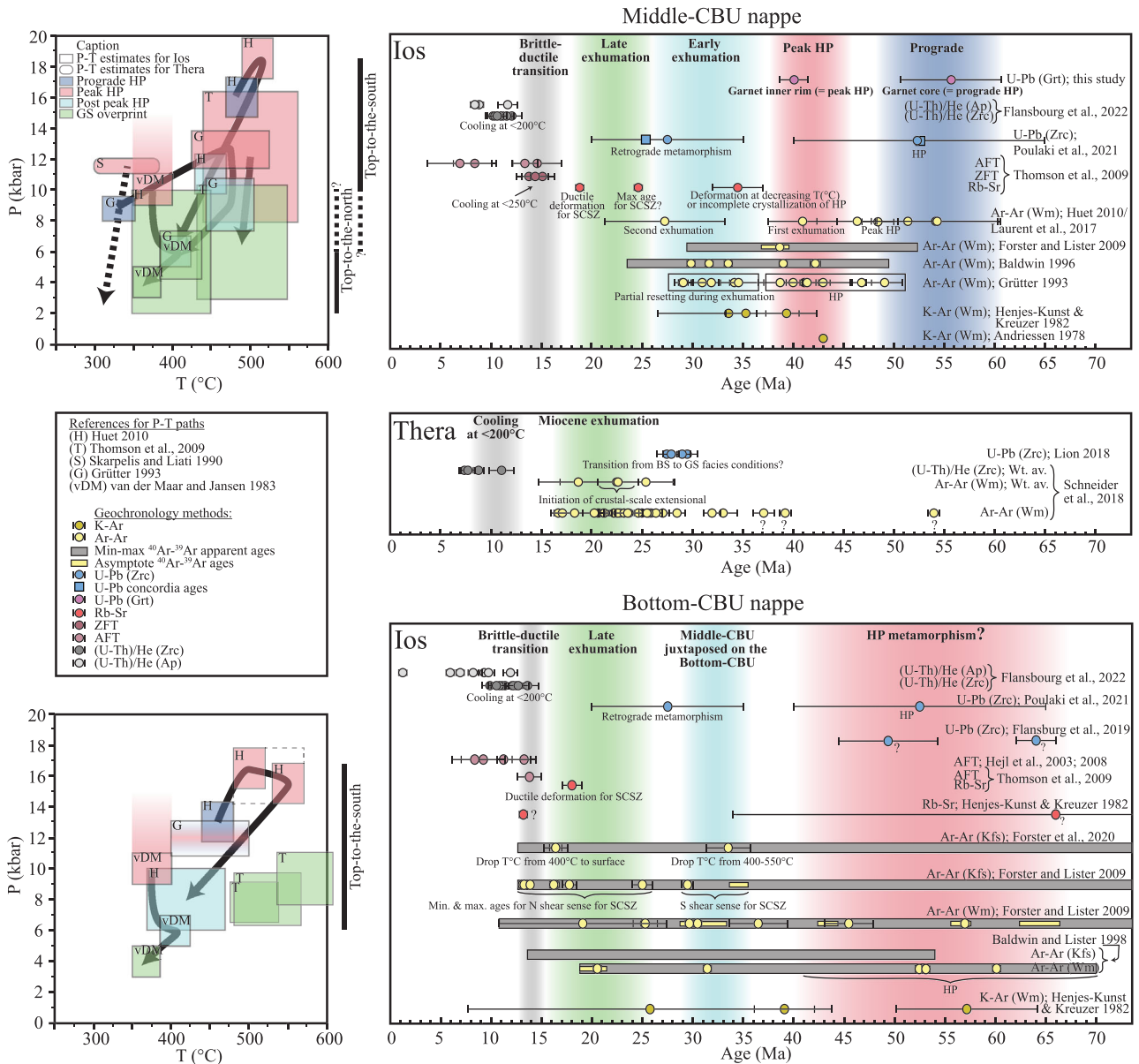


**FIGURE 4** Review of the pressure–temperature and geochronology data for the middle-CBU nappe and the bottom-CBU nappe on Ios and Thera. Interpretation of age data are labelled next to it. Interpretations from this paper are labelled in bold at the top of the geochronology figure. Ages older than 70 ma are not shown. In the age review tables, major interpretations from individual authors are below their data. Metamorphic event reinterpretations are labelled in bold at the top of the table. Colours corresponding to the age reinterpretations match colours presented in the corresponding P–T path. [Colour figure can be viewed at [wileyonlinelibrary.com](https://onlinelibrary.wiley.com/doi/10.1111/jmg.12753)]

estimated at 8–12 kbar and 425–475°C using avP-T and thermodynamic models (Grütter, 1993; Huet, 2010). A later greenschist facies overprint is associated with top-to-the-north shearing (Grütter, 1993; Huet et al., 2009; Thomson et al., 2009) and occurred at 2–10 kbar and 350–550°C, as evidenced by avP-T and thermodynamic models (Grütter, 1993; Huet, 2010; Thomson et al., 2009).

K-Ar and  $^{40}\text{Ar}/^{39}\text{Ar}$  white mica and zircon U-Pb geochronology show two age clusters at 52–48 and 45–38 Ma for HP metamorphism (Andriessen, 1978; Baldwin, 1996; Forster & Lister, 2009; Grütter, 1993; Henjes-Kunst &

Kreuzer, 1982; Kreuzer et al., 1978; Laurent et al., 2017; Poulaki et al., 2021). The timing of exhumation spans from c. 35 Ma to 18 Ma (e.g., see zircon U-Pb ages of Poulaki et al., 2021 – Figure 4). Within this large age spread, two clusters have been identified at 35–26 and 25–18 Ma from K-Ar and  $^{40}\text{Ar}/^{39}\text{Ar}$  step heating spectra of phengite, paragonite and K-feldspar (Baldwin, 1996; Grütter, 1993; Henjes-Kunst & Kreuzer, 1982). Forster and Lister (2009) use microstructures to explain complex  $^{40}\text{Ar}/^{39}\text{Ar}$  step heating patterns. They suggest that HP white mica dated at >39.7 Ma reequilibrated at c. 35 Ma

during top-to-the-south directed shearing at the SCSZ (which lasted for *c.* 5 Ma), followed by a second overprint during top-to-the-north shearing at *c.* 25 Ma. Thomson et al. (2009) report similar ages using multi-mineral Rb-Sr analyses. A  $34.5 \pm 2.5$  Ma age is interpreted as incomplete recrystallization of the HP assemblage. A poorly defined mixed age of *c.* 25 Ma is difficult to interpret and might be the maximum age for ductile normal movement at the SCSZ, the latter of which is well defined at *c.* 19–18 Ma when normal faulting is bivergent (top-to-the-N at the northern Middle/Bottom-CBU contact and top-to-the-S at the southern contact). Exhumation and cooling to shallow crustal levels associated with brittle deformation is recorded at  $14.4 \pm 2.5$  Ma (Thomson et al., 2009).

### 3.3 | Thera island

The geology of the island of Thera has been dominated by active volcanism since the Pleistocene. Remnants of the pre-volcanic rocks belong to the Middle-CBU nappe and the Pelagonian unit, which are separated by an early Miocene top-to-SSE detachment fault (Figure 2c – Schneider et al., 2018). The Middle-CBU nappe shows peak HP metamorphism at 11–12 kbar and 300–380°C (Figure 4 – Skarpelis & Liati, 1990). The age for the HP metamorphism is unknown. (U–Th)/He zircon ages constraining cooling to <200°C yielded 11–8 Ma (Schneider et al., 2018).

## 4 | SAMPLING STRATEGY AND METHODS

For Ios, existing P–T data are inconsistent, with differences in peak HP pressure estimates of about 6 kbar between *avP–T* (Grütter, 1993) and pseudo-section modelling (Huet, 2010). Such differences may result from chemical disequilibrium. Our first goal was to collect samples which record pristine metamorphic assemblages, including eclogite, blueschist and greenschist facies parageneses. Moreover, we collected samples that show incomplete mineral re-equilibration to understand the mineral reactions during prograde and retrograde metamorphism. We used similar methods for P–T estimations as previous authors (i.e., *avP–T* and pseudo-section modelling) to better interpret our P–T results and compare them with earlier results. Finally, we performed quartz-in-garnet barometry (QuiG) combined with Zr-in-rutile thermometry to obtain P–T data.

In-situ U–Pb garnet geochronology was carried out on garnet cores and rims to provide ages for both prograde and peak HP metamorphism and to link the ages

directly with the P–T estimates. On Thera, samples were collected at the same localities as those of previous workers (Schneider et al., 2018; Skarpelis & Liati, 1990). *AvP–T* and thermodynamic models were used to determine peak HP and subsequent P–T conditions. Analytical details of mineral chemistry, geothermobarometry, modelling and geochronology methods are reported in Supporting Information S1 and Table S12.

## 5 | SAMPLE DESCRIPTIONS

Four metasedimentary and mafic samples were collected from the Middle-CBU nappe on Ios and two on Thera. Coordinates, a brief sample description and detailed petrography are available in Supporting Information S2; paragenetic sequences are presented in Supporting Information S3.

### 5.1 | Ios

#### 5.1.1 | Slightly retrogressed eclogite (sample IO29)

Sample IO29 is characterized by sub-euhedral to euhedral garnet porphyroblasts (Figure 5a; Figure S1a–d – 100–800 μm). Garnet is anisotropic, indicating a non-cubic structure (Figure 5b). It shows variable compositions which are distinguished into core, inner rim and outer rim (Figure 6a,b; Table S1). The core contains inclusions of titanite, Na-amphibole, chlorite and apatite and its composition is rich in spessartine (Sps<sub>51–52</sub>), almandine (Alm<sub>20–24</sub>), grossular (Grs<sub>20–23</sub>) andradite (Adr<sub>2–4</sub>) and pyrope (Prp<sub><1</sub> – Figure 6a,b; Figure S1b,c; Table S1). From the core to the inner rim, spessartine and andradite decrease (Sps<sub>51–52</sub> to Sps<sub>8–10</sub>; Adr<sub>2–4</sub> to Adr<sub>1–2</sub>), while almandine and pyrope increase (Alm<sub>20–24</sub> to Alm<sub>63–65</sub>; Prp<sub><1</sub> to Prp<sub>3–4</sub>) and grossular remains constant. The inner rim contains ilmenite, Na-amphibole, omphacite, epidote and apatite inclusions (Figure 6a,b; Figure S1b,c). A locally observed narrow outer rim shows an increasing spessartine content, decreasing almandine and pyrope, with grossular and andradite contents similar to the inner rim (Alm<sub>50–52</sub>; Prp<sub>0–1</sub>; Grs<sub>20–23</sub>; Sps<sub>10–19</sub>; Adr<sub>1–2</sub> – Figure 6b; Figure 8).

Clinopyroxene (0.1–1 mm) has omphacite composition (Figure 7a; Table S2). Towards the rim, the jadeite content decreases (from Jd<sub>70</sub> to Jd<sub>36</sub>; Figure 7a). Two types of Na-amphibole are observed (Gln1 and Gln2). Gln1 is elongated (~1 cm long) along the foliation and contains inclusions of garnet (that only show core and inner rim), omphacite and ilmenite (Figure 5a,b,

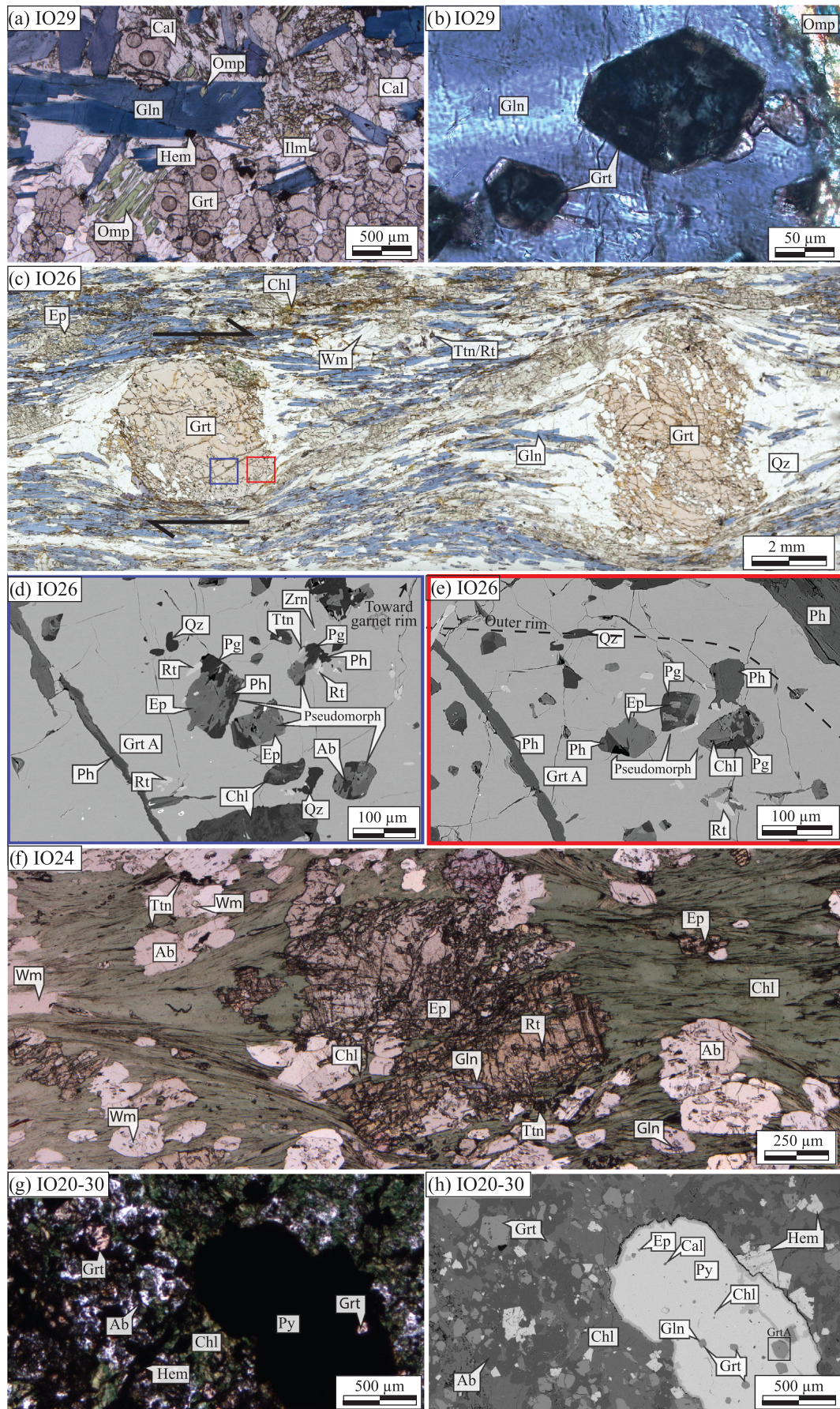


FIGURE 5 Legend on next page.

**FIGURE 5** Representative microstructures and metamorphic assemblages of rocks from Ios in plane- (PPL) and cross-polarized light (XPL) and SEM images. (a) PPL image of IO29. Location of laser spots used for U–Pb garnet age. (b) XPL image of IO29 showing anisotropic garnet porphyroblasts contained in glaucophane. (c) PPL panorama of sample IO26. (d and e) SEM image of IO26 showing typical assemblage of garnet core and rim, respectively. Note we observe pseudomorphs of white mica and epidote after lawsonite. (f) PPL image of IO24; rare glaucophane is observed in epidote porphyroclasts. (g and h) PPL and SEM images of IO20–30. HP assemblage is preserved in pyrite. Mineral abbreviations according to Whitney and Evans (2010). Ab = albite; Cal = calcite; Chl = chlorite; ep = epidote; Gln = glaucophane; Grt = garnet; hem = haematite; Ilm = ilmenite; Omph = omphacite; Pg = paragonite; Ph = phengite; Py = pyrite; Qz = quartz; Rt = rutile; Ttn = titanite; Wm = White mica; Zrn = zircon. [Colour figure can be viewed at [wileyonlinelibrary.com](http://wileyonlinelibrary.com)]

Figure 6a and Figure 8). Gln1 is also observed as an inclusion in garnet cores and inner rims. Gln2 is sub-euhedral to euhedral (1–5 mm), cross-cutting the foliation and contains inclusions of garnet (with outer rim), omphacite and ilmenite (Figure 8). From core to rim, the first type of Na-amphibole shows oscillatory compositional zoning. The  $\text{Fe}^{3+}/(\text{Fe}^{3+} + \text{Al}^{\text{VI}})$  and  $\text{Fe}^{2+}/(\text{Fe}^{2+} + \text{Mg})$  ratios decrease indicating a shift from riebeckite to ferroglaucophane towards the rim (Figure 7b; Table S3). A similar trend is observed for Na-amphibole inclusions in garnet. In contrast, the second type of Na-amphibole shows an increasing  $\text{Fe}^{3+}/\text{Fe}^{3+} + \text{Al}^{\text{VI}}$  ratio and a slightly decreasing  $\text{Fe}^{2+}/\text{Fe}^{2+} + \text{Mg}$  ratio from ferroglaucophane to riebeckite (Figure 7b; Table S3). Epidote inclusions in the garnet inner rim are rich in clinozoisite ( $\text{Czo}_{71}$ ; Table S4). Rare plagioclase ( $\text{Ab}_{99}$ ; Table S5), chlorite ( $X_{\text{Mg}} = 2.88$ ; Table S6) and calcite ( $X_{\text{cal}} = 0.95\text{--}0.97$ ; Table S7) are observed as inclusions in the garnet core and in pyrite. Haematite pseudomorphs after pyrite contain inclusions of garnet, omphacite and calcite (Figure S1e).

Slight retrogression in the blueschist facies is characterized by the formation of the garnet outer rim, Na-amphibole (Gln2), calcite, plagioclase, epidote, titanite and quartz (Figure 8; Table S1, S3–6). Calcite and quartz replace omphacite (Figures 5a and 8) while epidote and plagioclase replace Na-amphibole (Gln1) and garnet (Figure 6a). Titanite replaces ilmenite in the matrix and euhedral haematite grows near garnet and glaucophane (Figure 8; Figure S1e).

### 5.1.2 | Garnet-glaucophane schist (sample IO26)

Garnet porphyroblasts (3–5 mm) host inclusions of plagioclase, phengite, glaucophane, chlorite, rutile, titanite, zircon and pseudomorphs after lawsonite in the core (Figure 5c–e; Figure S2a, b). Towards the inner garnet rim, chlorite and plagioclase disappear (Figure 5d) and pseudomorphs after lawsonite are less abundant or absent. The outer rim contains inclusions of rutile and

quartz. The garnet core is rich in almandine ( $\text{Alm}_{47\text{--}49}$ ,  $\text{Prp}_{4\text{--}5}$ ,  $\text{Grs}_{17\text{--}19}$ ,  $\text{Sps}_{28\text{--}29}$ ; Figure 6c; Table S1). Towards the inner rim, almandine and pyrope contents increase ( $\text{Alm}_{55\text{--}57}$ ,  $\text{Prp}_{5\text{--}6}$ ) while the spessartine content decreases ( $\text{Sps}_{20\text{--}22}$ ). Grossular seems to initially decrease ( $\text{Grs}_{14\text{--}15}$ ) and then increase ( $\text{Grs}_{17\text{--}19}$ ) towards the inner rim (Figure 6c; Table S1). Na-amphibole has glaucophane composition (Figure 7c; Table S3). Glaucophane in the matrix shows a decrease in  $\text{Fe}^{3+}/(\text{Fe}^{3+} + \text{Al}^{\text{VI}})$  while  $\text{Fe}^{2+}/(\text{Fe}^{2+} + \text{Mg})$  increases from core to rim. Glaucophane inclusions in epidote and garnet show a similar compositional trend (Figure 7c; Table S3). In the garnet core and inner rim, epidote is often associated with paragonite or phengite, forming pseudomorphs after lawsonite (Figure 5d,e). The clinozoisite content decreases from  $\text{Czo}_{93\text{--}97}$  to  $\text{Czo}_{77\text{--}91}$  (Table S4) towards the rim. Epidote in the matrix contains glaucophane, paragonite, phengite, titanite, rutile and quartz inclusions (Figure S2c). Its chemical composition is similar to that of epidote inclusions in the garnet inner rim ( $\text{Czo}_{75\text{--}79}$ ; Table S4). Plagioclase is observed as inclusions in the garnet core and in the matrix. Its composition is almost pure albite (Table S5). White mica in the garnet core has paragonite and phengite compositions ( $\text{Si} = 3.11\text{--}3.12$  a.p.f.u.; Figure 7d). Towards the inner rim, the Si content of phengite increases to  $\text{Si} = 3.22\text{--}3.5$  a.p.f.u. (Figure 7d; Table S8). Comparable white micas are observed as inclusions in the epidote and as flakes in the matrix. Zirconium contents of rutile increase from rutile inclusions in the garnet core to those in the garnet outer rim (from 7 to 48 ppm; Table S10) indicating coeval growth of rutile and garnet. Chlorite is observed as inclusions in the garnet core until the mid-inner rim. Its composition is clinocllore/daphnite with  $X_{\text{Mg}} = 0.55\text{--}0.57$  (Table S6).

Garnet, white mica and glaucophane are slightly retrogressed. From the inner to the outer garnet rim, almandine and pyrope decrease ( $\text{Alm}_{48\text{--}49}$ ,  $\text{Prp}_3$ ) while grossular and spessartine increase ( $\text{Grs}_{22\text{--}23}$ ,  $\text{Sps}_{23\text{--}27}$ ; Figure 7c; Table S1). Phengite ( $\text{Si} = 3.35\text{--}3.42$  a.p.f.u.; Figure 7d; Table S8) overgrows paragonite in the matrix. Glaucophane is replaced by chlorite (Figure 5c). Secondary titanite is observed in the matrix.

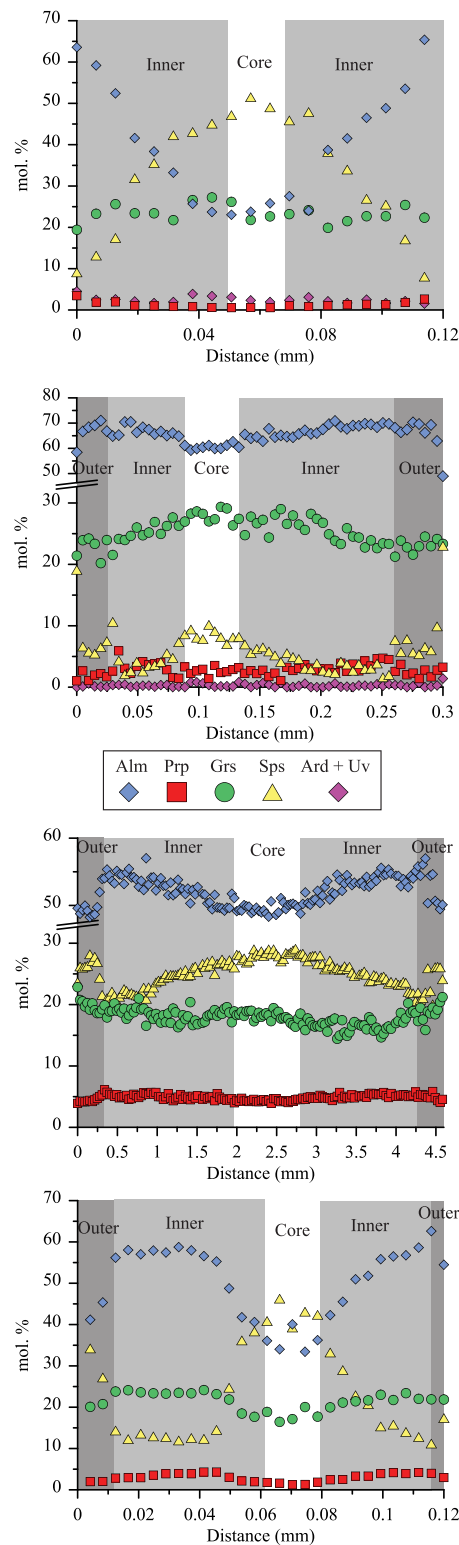
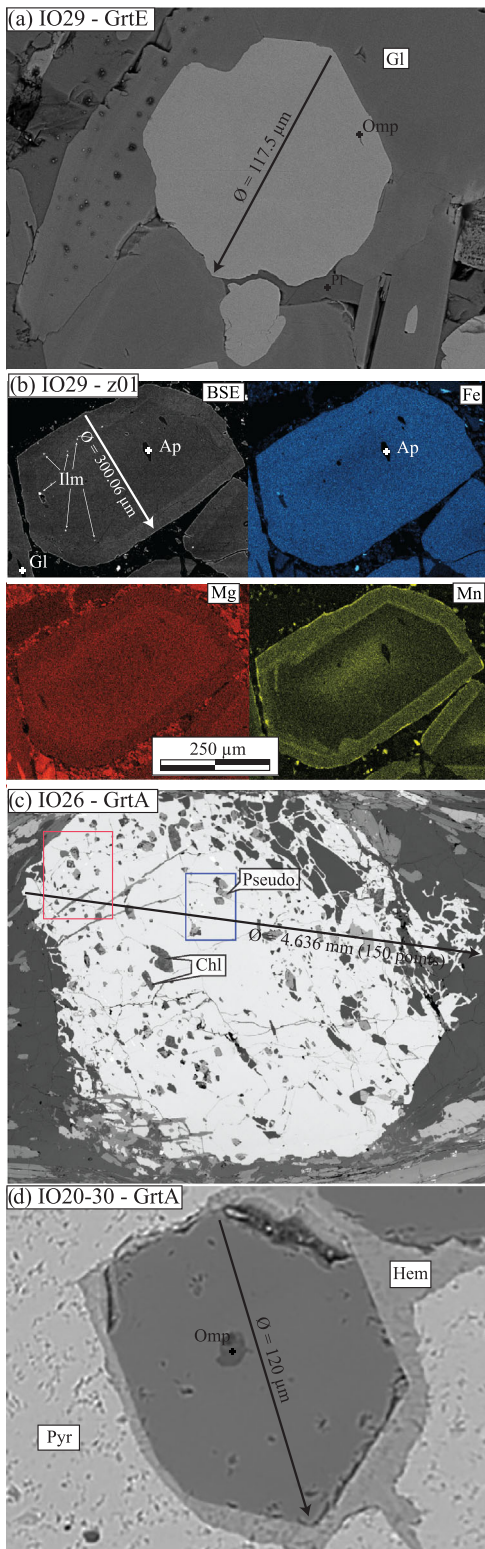


**FIGURE 6** Zoning profiles of representative garnet porphyroblasts and BSE images for IO29 (a, b), IO26 (c) and IO20–30 (d). [Colour figure can be viewed at [wileyonlinelibrary.com](https://onlinelibrary.wiley.com)]

### 5.1.3 | Chlorite schist with relict glaucophane (sample IO24)

The greenschist facies assemblage is composed of epidote, plagioclase, chlorite, white mica, calcite and titanite (Figure 5f; Figure S3a). Rare secondary epidote has a

similar composition to the rims of primary epidote ( $\text{Czo}_{73-75}$ ; Table S4). Secondary plagioclase in the matrix is albite (Table S5). Primary epidote was probably in an assemblage with albite and glaucophane and is partially replaced by chlorite (Figure 5f; Figure S3b–d) with a clinchlore/daphnite ( $X_{\text{Mg}} = 0.57-0.60$ ) composition

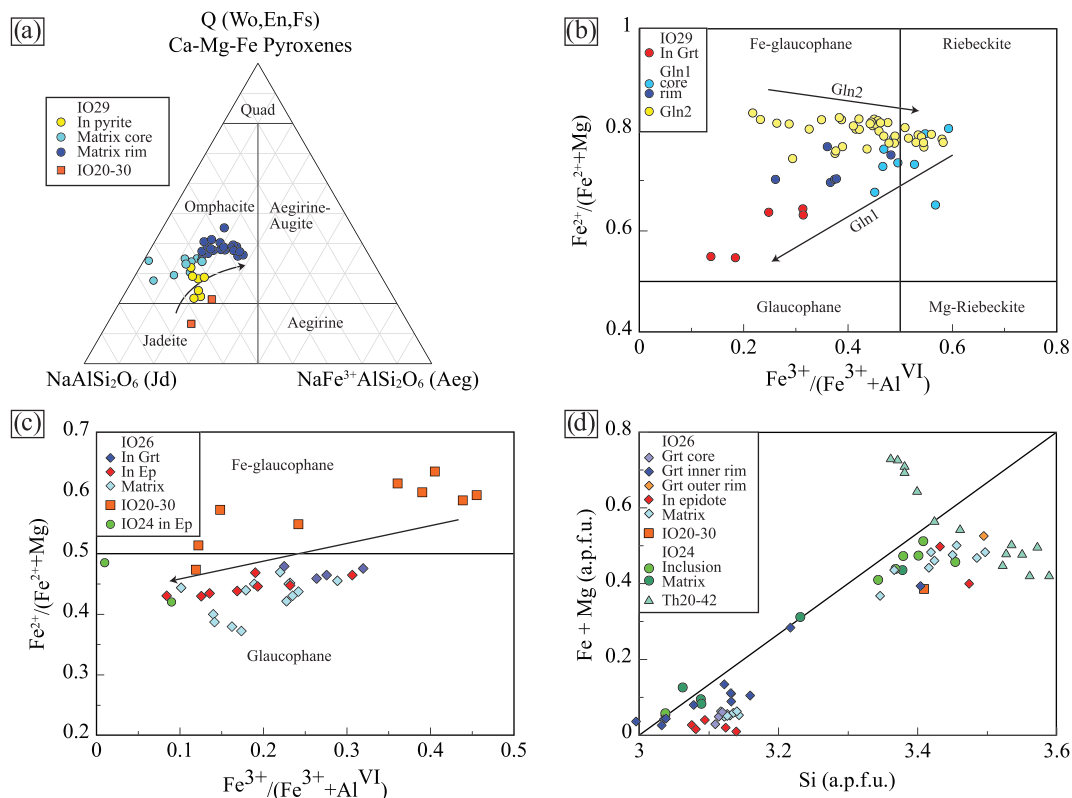


FIGURE 7 (a) Composition of clinopyroxene in IO29 and IO20-30 (Morimoto et al., 1988). (b) Composition of sodic amphibole of IO29. (c) Composition of sodic amphibole of IO26 and IO24 (Okay, 1980). (d) Si v. (Fe + mg) diagram illustrating phengite composition of IO26, IO20-30, IO24 and Th20-42. [Colour figure can be viewed at [wileyonlinelibrary.com](http://wileyonlinelibrary.com)]

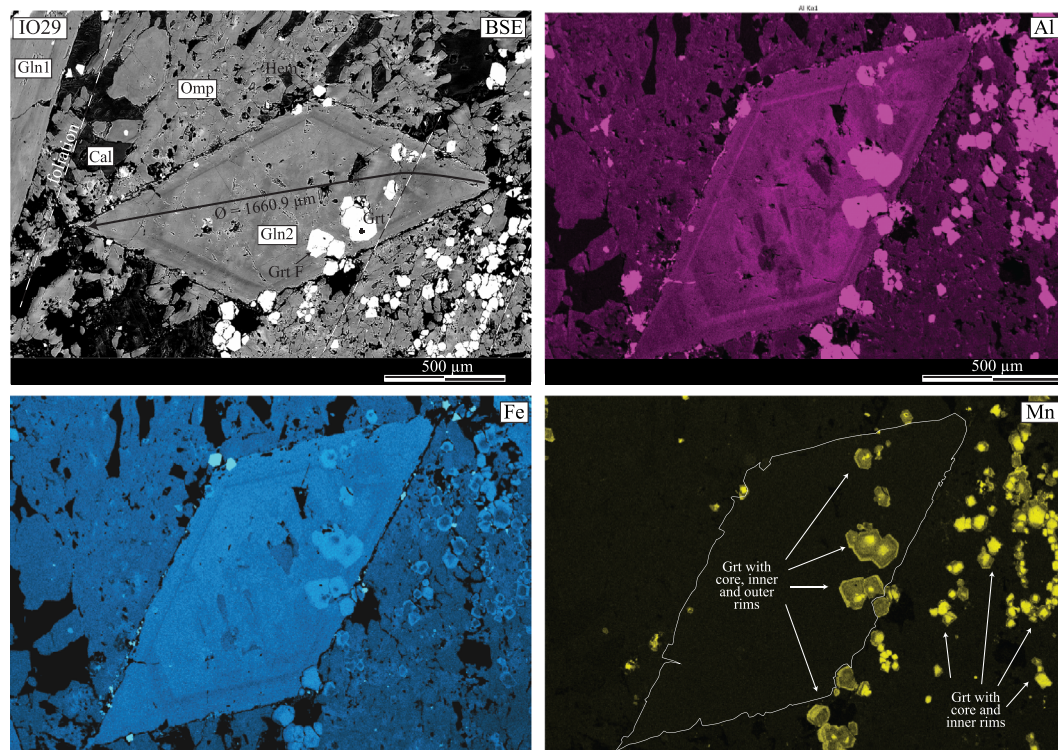


FIGURE 8 SEM images and zoning maps of a late Na-amphibole (Gln2) that hosts garnet showing an outer rim whereas garnet in the omphacite matrix does not show an outer rim. [Colour figure can be viewed at [wileyonlinelibrary.com](http://wileyonlinelibrary.com)]

(Table S6). White mica in the matrix and as inclusions in secondary albite are phengite ( $\text{Si} = 3.4\text{--}3.5$  a.p.f.u.) and muscovite (Figure 7d; Table S8). Calcite in the matrix is likely formed at the expense of primary epidote. Rutile is rimmed by titanite (Figure S3b,c).

High-pressure assemblages consisting of plagioclase, white mica, Na-amphibole and rutile are preserved as inclusions in epidote cores (Figure 5f) and in haematite pseudomorphically replacing former pyrite (Figure S3c). Na-amphibole in epidote rim and albite is glaucophane (Figure S3b-e), similar in composition to amphibole inclusion in garnet and epidote from IO26 (Figure 7c; Table S3). Epidote enclosed by haematite pseudomorph after pyrite is clinozoisite ( $\text{Czo}_{98-99}$ ; Figure S3c; Table S4). For epidote porphyroblast in the matrix the clinozoisite content decreases from  $\text{Czo}_{78-90}$  to  $\text{Czo}_{73-75}$  from core to rim. Plagioclase enclosed by pyrite is pure albite. Two types of white mica are observed as inclusions in haematite pseudomorph after pyrite and in epidote which have phengite ( $\text{Si} = 3.2\text{--}3.4$  a.p.f.u.) and paragonite compositions, respectively (Figure 7d; Figure S3c,d; Table S8). Rutile is observed as an inclusion in pyrite and epidote (Figure S3b-d).

#### 5.1.4 | Strongly retrogressed eclogite (sample IO20–30)

The preserved HP pressure assemblage consists of garnet, epidote, Na-amphibole, clinopyroxene, calcite and pyrite (Figure 5g,h; Figure 7d and Figure S4a-d). Garnet is observed in the matrix and as inclusion in pyrite (Figure 5g,h and Figure S4a,b). Compositional profiles indicate a core, an inner rim and an outer rim (Figure S4b). Core and inner rim are similar in composition to those of garnet in IO29 (core:  $\text{Alm}_{25-30}$ ,  $\text{Prp}_{1-2}$ ,  $\text{Grs}_{17-22}$ ,  $\text{Sps}_{45-50}$ ,  $\text{Adr}_{2-4}$ ; inner rim:  $\text{Alm}_{58-62}$ ,  $\text{Prp}_{2-4}$ ,  $\text{Grs}_{21-23}$ ,  $\text{Sps}_{10-11}$ ,  $\text{Adr}_{1-3}$ ; Figure 6d; Table S1). Clinopyroxene is observed as inclusion in garnet core, whereby the garnet occurs itself as inclusion in a pyrite core. The clinopyroxene composition is jadeite ( $\text{Jd}_{53-63}$ ; Figure 7a; Table S2). Na-amphibole is preserved as an inclusion in garnet and pyrite. From pyrite core to rim, Na-amphibole shows decreasing  $\text{Fe}^{3+}$  and  $\text{Fe}^{2+}$  that indicate a shift from riebeckite to ferroglaucophane/glaucophane (Figure 7c; Table S3). Na-amphibole inclusions in garnet are glaucophane. Epidote inclusions in pyrite show a similar composition to those in the garnet inner rim of IO29 ( $\text{Czo}_{67-69}$ ; Table S4). Calcite is observed in the matrix (Figure S4d) and as inclusion in pyrite and garnet core. A Mg- and Fe-rich calcite composition ( $X_{\text{Sid}} = 0.14\text{--}0.17$ ;  $X_{\text{Dol}} = 0.29\text{--}0.31$ ; Table S7) was analysed for carbonate inclusions in garnet.

Early retrogression in sample IO20–30 is evidenced by inclusion assemblages in the pyrite rim and in garnet. The outermost garnet rim shows an increasing spessartine ( $\text{Sps}_{10-19}$ ) and decreasing almandine and pyrope ( $\text{Alm}_{50-52}$ ;  $\text{Prp}_{0-1}$ ) content, while grossular and andradite remain constant (Figure 6d; Table S1). Na-Ca amphibole inclusions in pyrite have a ferro-winchite composition (Table S3). Later retrogression at greenschist facies conditions formed a chlorite, plagioclase, calcite and haematite assemblage (Figure 5g,h and Figure S4). Omphacite, glaucophane and partly also garnet broke down to chlorite, plagioclase, calcite and epidote. Epidote in the matrix has a composition close to that of epidote inclusions in pyrite ( $\text{Czo}_{70-71}$ ; Table S4). Plagioclase is albite (Table S5).  $X_{\text{Mg}}$  of chlorite varies between 0.54 and 0.65 (Table S6). The carbonate is calcite (Table S7). Rare white mica in the matrix is phengite ( $\text{Si} = 3.39$  a.p.f.u.) (Figure 7d; Table S8). Pyrite edges are dissolved with haematite grown on them and as isolated grains in the matrix (Figure 5h).

#### 5.1.5 | Thera

##### 5.1.6 | Greenschist facies quartzite (sample Th20–42)

Th20–42 is a quartzite which contains quartz, together with white mica, chlorite, feldspar, rutile, apatite and monazite (Figure 9a and Figure S5a-c). Folded feldspar ribbons and ribbons of quartz form centimetre-scale folds (Figure 9a). Two types of feldspar, albite and alkali feldspar, are observed (Figure 9b; Figure S5c; Table S5), which are in textural equilibrium.  $X_{\text{Mg}}$  of chlorite varies between 0.60 and 0.67 (Table S6). White mica is intergrown with chlorite (Figure 9b and Figure S5b,c). The Si content of white mica ranges between 3.3 and 3.6 a.p.f.u. (Figure 7d; Table S8). Large rutile shows a skeleton-like shape with porosity filled with chlorite, plagioclase and white mica (Figure 9c and Figure S5b). This texture indicates the dissolution of magmatic ilmenite and its replacement by metamorphic rutile (Angiboust & Harlov, 2017).

##### 5.1.7 | Pumpellyite facies metabasalt (sample Th06)

Th06 is a metabasalt rock which contains chlorite, feldspar, pumpellyite, Ca-amphibole, calcite, white mica, titanite and quartz aligned along the foliation (Figure 9d,e and Figure S6a-c). Relics of the magmatic assemblages are characterized by fragments of porphyroclastic clinopyroxene (Figure 9d,e and Figure S6a-c). Chlorite, white mica and albite replace the pyroxene (Figure 9d and



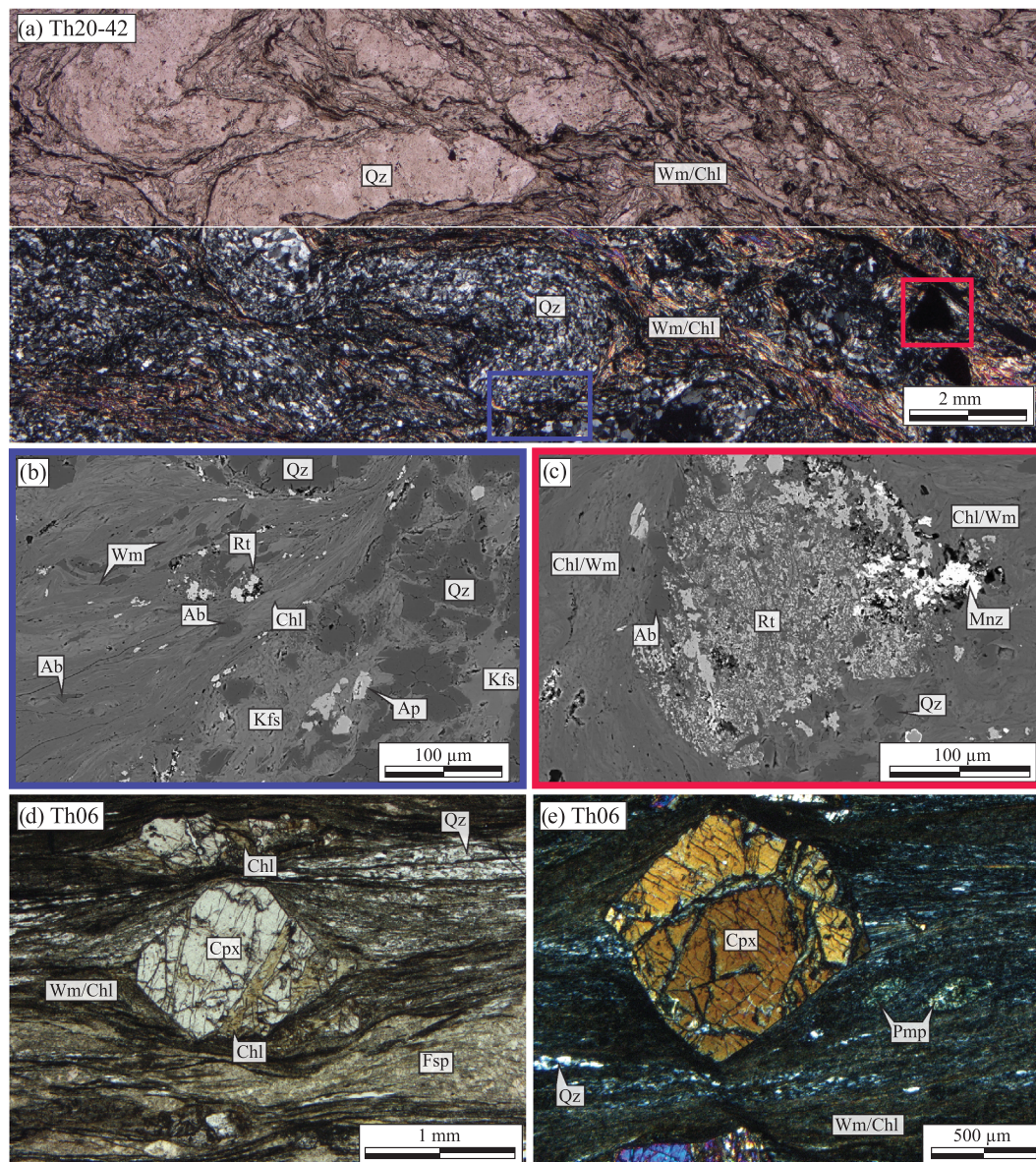


**FIGURE 9** (a) Representative photograph showing metamorphic assemblages of Th20–42 from Thera in plane- (PPL) and cross-polarized light (XPL). (b & c) SEM images of close-up view of (a) showing interlayers of chlorite, white mica and quartz. Mineral abbreviations according to Whitney and Evans (2010). Ab = albite; Ap = apatite; Chl = chlorite; Cpx = clinopyroxene; Mnz = monazite; Pmp = pumpellyite; Qz = quartz; Rt = rutile; Wm = White mica. [Colour figure can be viewed at [wileyonlinelibrary.com](https://onlinelibrary.wiley.com/doi/10.1111/jmg.12753)]

Figure S6b,c). They are similar in composition to those of sample Th20–42 (Tables S5, S6 and S8). Pumpellyite forms elongated roundish grains aligned parallel to the foliation (Figure 9e and Figure S6b). Its composition is Al-rich with an  $X_{Mg}$  of 0.53–0.89 (Table S9). Ca-amphibole is magnesio-hornblende and edenite (Table S3).

## 6 | P–T RESULTS

For the eclogite and blueschist facies samples from Ios, distinct P–T estimates were obtained from (1) mineral inclusions in garnet core (prograde), (2) mineral

inclusions in garnet inner rim (peak HP metamorphism), (3) inclusions in garnet outer rim and matrix minerals (post-peak HP metamorphism) and (4) matrix minerals (greenschist facies overprint). Equilibrium is indicated by multiphase inclusions.

### 6.1 | Average P–T

#### 6.1.1 | Ios island

According to the metamorphic assemblages defined in section 5.1, the prograde mineral assemblage in eclogite

**TABLE 1** Summary of P–T–t estimates from average P–T, thermodynamic models and geobarometry based on Zr-in-rutile thermometry and quartz-in-garnet barometry. U–Pb garnet ages are reported for prograde and peak HP metamorphism.

Metamorphic stage	Sample	Average P–T				Geothermobarometry (QuiG & Zr-in-Rt)				
		T (°C)	± (2σ)	P (kbar)	± (2σ)	Corr.	Sigfit	T (°C)	± (2σ)	P (kbar)
<b>Ios</b>										
Prograde	IO29	326	20	6.7	1.4	0.82	1.06/1.54	-	-	-
(Garnet core)	IO26	467	42	10.5	2.0	0.98	1.24/1.54	460	14	10.3
Peak HP	IO29	472	30	11.6	3.0	0.84	0.99/1.54	-	-	-
(Garnet inner rim)	IO26	531	36	11.9	1.8	0.64	1.47/1.49	501	34	13.2
Post peak HP	IO29	478	34	9.0	1.8	0.85	1.24/1.54	-	-	-
(Garnet outer rim)	IO26	462	20	9.7	1.6	0.91	1.16/1.42	473	15	10.8
GS facies	IO26	-	-	-	-	-	-	-	-	-
(Garnet out)	IO20–30	416	46	4.8	2.4	0.96	1.33/1.73	-	-	-
	IO24	409	34	4.9	2.0	0.97	0.97/1.73	-	-	-
<b>Thera</b>										
Peak HP	Th20–42	-	-	-	-	-	-	-	-	-
	Th06	361	18	7.6	1.6	0.71	0.51/1.96	-	-	-
Post peak HP	Th20–42	-	-	-	-	-	-	-	-	-

TABLE 1 (Continued)

Metamorphic stage	Geothermobarometry (QuiG & Zr-in-Rt)			Thermodynamic models					Age (ma) ± (2σ)	
	± (2σ)	Corr.	Nb. Inters.	T (°C)	± (2σ)	P (kbar)	± (2σ)	Corr.		Nb. Inters.
<b>Ios</b>										
Prograde	-	-	-	-	-	-	-	-	-	55.7 ± 5.0
(Garnet core)	1.2	0.40	18	480	38	13.5	1.6	-0.90	4	-
Peak HP	-	-	-	-	-	-	-	-	-	-
(Garnet inner rim)	1.1	0.42	48	561	48	15.9	3.0	-0.71	4	40.1 ± 1.4
Post peak HP	-	-	-	-	-	-	-	-	-	-
(Garnet outer rim)	1.2	0.38	27	555	25	10.0	1.0	0.53	12	-
GS facies	-	-	-	~430	-	~5-7	-	-	2	-
(Garnet out)	-	-	-	-	-	-	-	-	-	-
	-	-	-	-	-	-	-	-	-	-
<b>Thera</b>										
Peak HP	-	-	-	~300	-	~7.5	-	-	2	-
	-	-	-	-	-	-	-	-	-	-
Post peak HP	-	-	-	~275	-	~2.0	-	-	-	-

sample IO29 is represented by inclusions of glaucophane, clinopyroxene, epidote, plagioclase, chlorite, titanite and calcite in glaucophane and garnet core. These minerals define P–T conditions of  $326 \pm 20^\circ\text{C}$  and  $6.7 \pm 1.4$  kbar ( $X_{\text{CO}_2} = 0.001$ ; see method section). In garnet glaucophane schist IO26, the prograde assemblage comprises inclusions of glaucophane, paragonite, chlorite, plagioclase, lawsonite and rutile as inclusions in garnet core and yields  $467 \pm 42^\circ\text{C}$  and  $10.5 \pm 2$  kbar (Table 1; Figure 10a).

P–T conditions of peak HP metamorphism on Ios are defined by glaucophane, omphacite, epidote, calcite and ilmenite inclusions in the garnet inner rim. For the calcite-bearing eclogite sample IO29 peak P–T is calculated for a mixed  $\text{H}_2\text{O}/\text{CO}_2$  fluid with  $X_{\text{CO}_2} = 0.008$  and yields  $472 \pm 30^\circ\text{C}$  and  $11.6 \pm 3.0$  kbar. For the garnet-glaucophane schist IO26 the peak metamorphic assemblage of glaucophane, epidote, phengite, chlorite, plagioclase and rutile, preserved as inclusions in garnet inner rim yields  $531 \pm 36^\circ\text{C}$  and  $11.9 \pm 1.8$  kbar.

Post-peak HP metamorphic conditions of the eclogite sample IO29 are calculated for the assemblage of the garnet outer rim and inclusions of glaucophane, epidote, plagioclase, carbonate and haematite using a mixed  $\text{H}_2\text{O}/\text{CO}_2$  fluid with  $X_{\text{CO}_2} = 0.02$ . The P–T calculation yields  $478 \pm 32^\circ\text{C}$  and  $9.0 \pm 1.8$  kbar. Retrograde P–T conditions calculated for the garnet-glaucophane schist IO26 are  $462 \pm 20^\circ\text{C}$  and  $9.7 \pm 1.8$  kbar using the assemblage of garnet outer rim and inclusions of glaucophane, paragonite, phengite, plagioclase, calcite, rutile and titanite, assuming a  $X_{\text{CO}_2} = 0.01$  of the fluid (Table 1; Figure 10a).

The greenschist facies overprint for IO20–30 and IO24 is calculated from albite, chlorite, epidote, white mica, calcite, titanite and haematite of the matrix and a  $\text{H}_2\text{O}/\text{CO}_2$  fluid with  $X_{\text{CO}_2} = 0.01$ . P–T estimates yield consistent

values of  $416 \pm 46^\circ\text{C}$  and  $4.8 \pm 2.4$  kbar and  $409 \pm 34^\circ\text{C}$  and  $4.9 \pm 2$  kbar, respectively (Table 1; Figure 10a).

### 6.1.2 | Thera island

For Th06, peak metamorphism is calculated from white mica, chlorite, amphibole, pumpellyite, carbonate and titanite assuming a mixed  $\text{H}_2\text{O}/\text{CO}_2$  fluid with  $X_{\text{CO}_2} = 0.001$  and gives  $361 \pm 18^\circ\text{C}$  and  $7.6 \pm 1.8$  kbar (Table 1; Figure 10a).

## 6.2 | Zr-in-rutile thermometry and QuiG barometry, Ios Island

Quartz and rutile inclusions in the garnet cores of eclogite sample IO26 record  $10.3 \pm 1.2$  kbar and  $460 \pm 14^\circ\text{C}$  (Figure 10b; Table 1 and Tables S10 and S11). Quartz and rutile inclusions in the inner garnet rim indicate increasing P–T values reaching peak HP conditions at  $13.2 \pm 1.1$  kbar and  $501 \pm 34^\circ\text{C}$ . Quartz and rutile inclusions within the garnet outer rim, record retrograde P–T conditions of  $10.8 \pm 1.2$  kbar and  $473 \pm 15^\circ\text{C}$ .

## 6.3 | Thermodynamic modelling, Ios Island

Pressure temperature values constrained for eclogite sample IO26 calculated from equilibrium phase diagrams are inconsistent with avP–T and combined Zr-in-rutile thermometry and QuiG barometry. Results and discussion are provided in Table 1; Figure 10c and Figure S7.

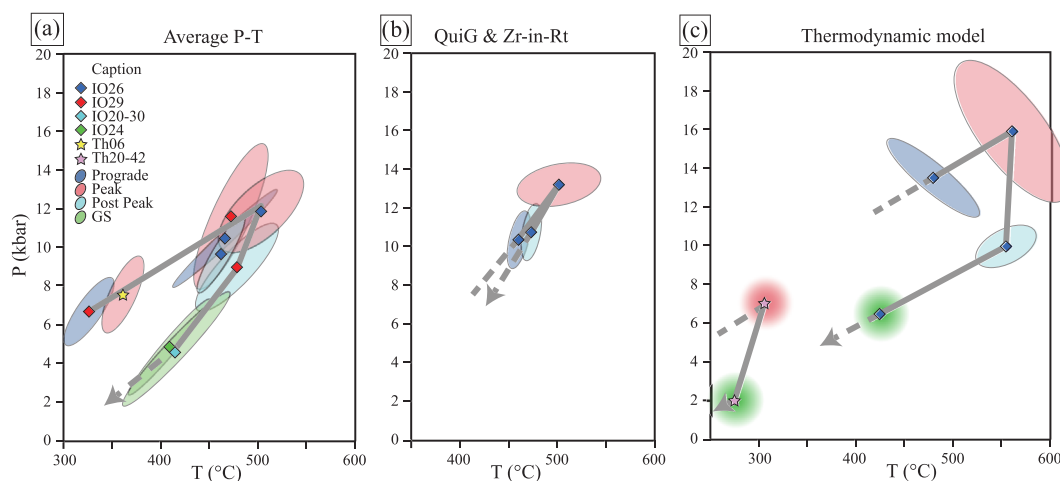


FIGURE 10 Comparison between avP–T, QuiG & Zr-in-rutile and thermodynamic model methods for samples from Ios and Thera. [Colour figure can be viewed at [wileyonlinelibrary.com](http://wileyonlinelibrary.com)]

In contrast, the calculation of equilibrium phase diagrams for the greenschist facies quartzite sample Th20–42 gives reasonable results. The stability fields corresponding to the peak HP assemblage indicate P–T conditions of  $\sim 280$ – $450^\circ\text{C}$  and  $\sim 7$ – $9$  kbar, which fit well with the values obtained by average P–T. More precise peak P–T values are estimated for the analysed composition of texturally early chlorite ( $X_{\text{Mg}} = 0.65$ ) and phengite ( $\text{Si} = 3.3$  a.p.f.u.). The two isopleths nearly intercept at  $\sim 300^\circ\text{C}$  and  $\sim 7.5$  kbar (Table 1; Figure 10b; Figure S7). P–T conditions for post-peak retrogression are  $\sim 275^\circ\text{C}$  and  $\sim 2$  kbar, using the composition of texturally late chlorite ( $X_{\text{Mg}} = 0.62$ ) and muscovite ( $\text{Si} = 3.24$  a.p.f.u.).

## 7 | IN-SITU U–PB GARNET GEOCHRONOLOGY, IOS ISLAND

Due to the small grain size of the garnets in eclogite sample IO29 (100–500  $\mu\text{m}$ ) and the large diameter of the laser spot (130  $\mu\text{m}$ ), the narrow garnet rims could not be dated. U–Pb spot analyses hence aimed at garnet cores showing elevated Mn contents. Detailed SEM–EDX and microprobe–WDX element transects and maps were performed for these garnets in advance to make sure that the central section of the core is analysed and to prevent sectioning effects. For the garnet–glaucophane schist IO26, garnets were large enough ( $>4$  mm) to date both the garnet core and inner rim. Due to the narrow size of the garnet outer rims, no U–Pb age could be constrained.

U–Pb data of garnet core analysis for IO29 define an unanchored regression line with a lower intercept age of  $55.7 \pm 5.0$  Ma ( $\pm 2\sigma$ , MSWD = 0.90) in the Tera–Wasserburg diagram (Figure 11a). The U and Pb contents of the garnet are highly variable, between 1 and 190 ng/g

and 3 ng/g and 1.25  $\mu\text{g/g}$ , respectively, with a maximum  $^{238}\text{U}/^{206}\text{Pb}$  ratio of  $c. 50$ . The determined lower intercept age corresponds to prograde HP metamorphism.

Due to the low U signal, it was not possible to perform analyses in the garnet cores of sample IO26. In the garnet inner rim, the U content for single spots varies from 1 to 150 ng/g, except for two spots where the U content is  $>500$  ng/g. Although inclusions were avoided, this distinctively higher U content may reflect some invisible U-rich inclusions (likely rutile) that were hit during deep profiling. The Pb content is low, with a maximum amount of 14 ng/g. The data, excluding the two U-rich values, define a regression line with a lower intercept at  $42.1 \pm 6.6$  Ma (MSWD = 0.72) in the Tera–Wasserburg diagram (Figure 11b). Including the U-rich data (green ellipses in Figure 11b), the spread on the  $^{238}\text{U}/^{206}\text{Pb}$  ratio increases up to  $c. 130$  and a more precise lower intercept age of  $40.1 \pm 1.4$  Ma (MSWD = 0.87) is obtained. In any case, the fact that both ages are similar within error indicates that the presumed inclusions are formed coeval with garnet growth. This interpretation is also supported by Zr-in-rutile thermometry, which indicates equilibrium and thus points to the coeval growth of rutile and garnet. The obtained age thus reflects peak HP metamorphism for this sample.

## 8 | STRUCTURAL RECONSTRUCTION OF THE CBU NAPPE

### 8.1 | Middle-CBU nappe: Naxos island

The review of the P–T–t data presented in this study for Naxos Island indicates two different P–T–t paths for the lower and the upper part of the Middle-CBU nappe. For

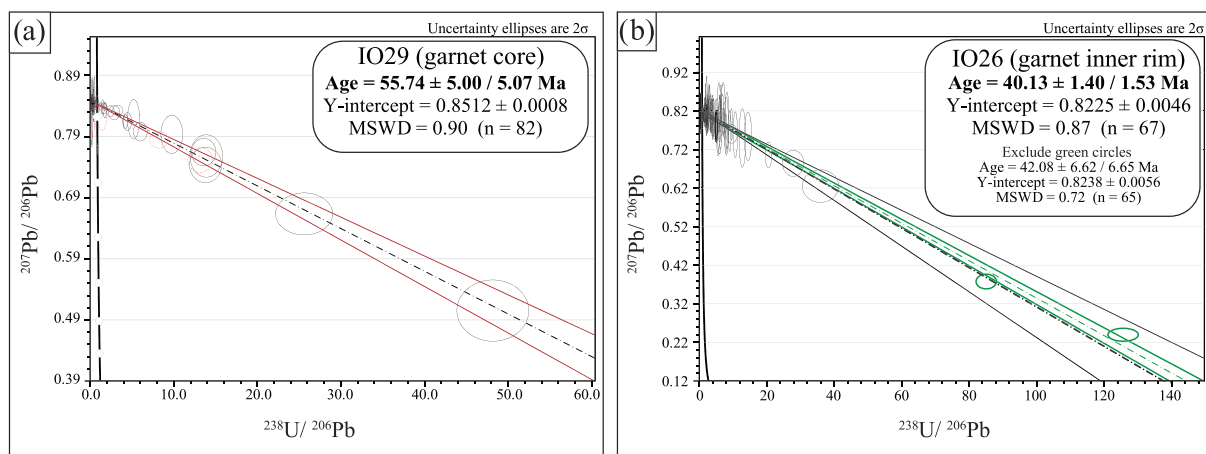


FIGURE 11 U–Pb Tera–Wasserburg diagrams for a) garnet core in IO29; b) garnet inner rim in IO26. Note that the Y-intercept refers to the initial  $^{207}\text{Pb}/^{206}\text{Pb}$  composition. See text for further details. [Colour figure can be viewed at [wileyonlinelibrary.com](http://wileyonlinelibrary.com)]

the model presented in this study, the data and interpretations of Martin (2004) and Peillod, Majka, et al. (2021); Peillod, Tehler, and Ring (2021) are used. Following these data, the lower part of the Middle-CBU nappe, close to the Bottom-CBU nappe, experienced prograde and peak HP conditions of  $15.4 \pm 0.8$  kbar and  $496 \pm 16^\circ\text{C}$  to  $19.9 \pm 0.6$  kbar and  $572 \pm 7^\circ\text{C}$  respectively (Figure 13). Our age review shows that peak HP metamorphism occurred at 46–38 Ma. Ages for the prograde P–T evolution, on the other hand, are more difficult to determine. For three samples used for P–T determination (samples NA0180b; NA0262b and NA01113b in Martin, 2004) and located in the lower part of the Middle-CBU nappe of Naxos, Martin et al. (2006) distinguish two clusters of Eocene U–Pb zircon ages, i.e.  $54.5 \pm 6.5$  Ma and  $44 \pm 3$  Ma, which broadly correspond to our new U–Pb garnet ages obtained for Ios. For these Naxos samples,  $\delta^{18}\text{O}$  isotope data suggest coeval growth of zircon and garnet during the Eocene (Martin et al., 2006). This interpretation is supported by our petrological observations of zircon inclusions in garnet from both Ios (this study) and Naxos (Peillod, Majka, et al., 2021). Therefore, we suggest that the U–Pb zircon age of  $54.5 \pm 6.5$  Ma is a good estimation for a prograde metamorphic stage and corresponds to the P–T estimate of  $15.4 \pm 0.8$  kbar and  $496 \pm 16^\circ\text{C}$ .

Early exhumation to  $8.3 \pm 1.5$  kbar,  $519 \pm 12^\circ\text{C}$  occurred at 35–29 Ma and was followed by isobaric heating of  $\sim 50$ – $100^\circ\text{C}$ . Isobaric heating lasted c. 10 Ma (Peillod, Majka, et al., 2021) and was followed by late near-isothermal decompression from  $9.2 \pm 0.8$  kbar and  $550 \pm 10^\circ\text{C}$  to  $3.8 \pm 0.3$  kbar and  $520 \pm 4^\circ\text{C}$  until 14–12 Ma.

The upper part of the Middle-CBU nappe (S-Naxos) experienced peak HP conditions of  $15.9 \pm 0.7$  kbar and  $597 \pm 22^\circ\text{C}$  (Figure 13) at c. 42–38 Ma (Peillod et al., 2017). The greenschist facies overprint at  $3.8 \pm 1.1$  kbar and  $384 \pm 30^\circ\text{C}$  occurred at  $32 \pm 3$  Ma, constraining near-isothermal decompression at c. 38–32 Ma (Avigad, 1998; Peillod et al., 2017). Zircon FT ages range from 25 Ma at the top of the sequence to 7 Ma at the bottom, indicating that rocks on Naxos progressively crossed the brittle-ductile transition during this period (Seward et al., 2009).

## 8.2 | Middle-CBU nappe: Ios island

Our new data provide P–T–t data for the prograde metamorphic evolution of the Middle-CBU nappe of Ios at  $6.7 \pm 1.4$  kbar,  $326 \pm 20^\circ\text{C}$  and  $55 \pm 5$  Ma, recorded by cores of Mn-rich garnet in eclogite (Figures 4 and 12). The rocks experienced subsequent peak HP metamorphism at  $40.1 \pm 1.4$  Ma (U–Pb garnet inner rim) at P–T of  $13.0 \pm 1.6$  kbar

and  $506 \pm 13^\circ\text{C}$ , based on a weighted average of the P–T values. Prograde and peak P–T estimates are in agreement with those obtained by Grütter (1993). The large spread of U–Pb garnet ages for prograde and peak metamorphism on Ios might also explain the large scatter of U–Pb zircon ages (65–40 Ma) reported from similar rocks by Poulaki et al. (2021). It is possible that the large range of U–Pb zircon ages corresponds to two distinct episodes of zircon growth, i.e. prograde and peak, as is also speculated for similar zircon age ranges recorded on Naxos (Martin et al., 2006).

Post-peak HP metamorphism is estimated at  $10.1 \pm 0.6$  kbar and  $484 \pm 14^\circ\text{C}$  and followed by exhumation to greenschist facies conditions of  $5.7 \pm 1.2$  kbar and  $416 \pm 14^\circ\text{C}$  (Figure 12). This metamorphic stage is geochronologically unconstrained. However, available  $^{40}\text{Ar}/^{39}\text{Ar}$  age data indicate two metamorphic events following HP peak metamorphism at c. 31 and c. 25 Ma (Baldwin, 1996; Forster & Lister, 2009; Grütter, 1993). The age of c. 31 Ma is interpreted to date top-to-the-south shearing along the SCSZ whereas the c. 25 Ma age is interpreted to date the onset of the greenschist facies overprint (Forster et al., 2020; Forster & Lister, 2009). Forster et al. (2020) show that these two ages correspond to two episodes of cooling from  $\sim 550$  to  $\sim 400^\circ\text{C}$  and from  $\sim 400^\circ\text{C}$  to the ductile-brittle transition, respectively. P–T estimates indicate that at  $400^\circ\text{C}$  the rocks were

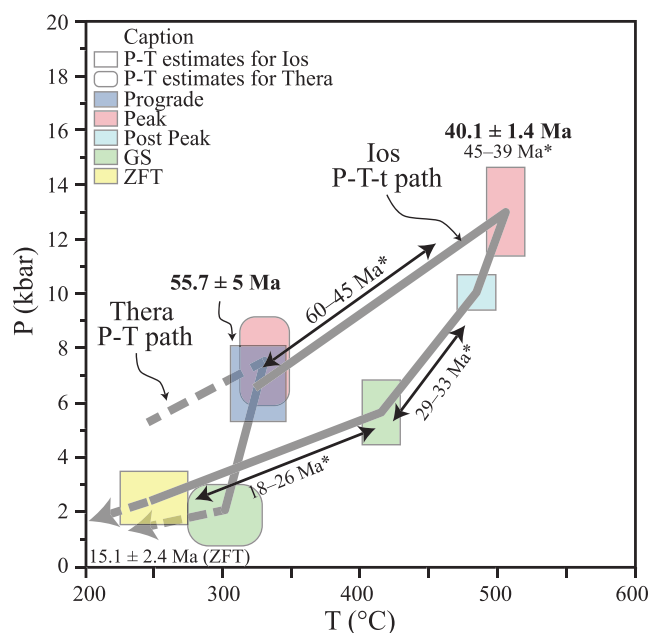


FIGURE 12 Summary of P–T–t path for Ios and Thera. Age data in bold are from garnet U–Pb ages and age data with \* are a compilation of available data (Baldwin, 1996; Forster & Lister, 2009; Grütter, 1993; Henjes-Kunst & Kreuzer, 1982; Poulaki et al., 2021; Thomson et al., 2009). [Colour figure can be viewed at [wileyonlinelibrary.com](http://wileyonlinelibrary.com)]

exhumed to  $\sim 5$  kbar. Therefore, the rocks were in the upper middle crust at *c.* 31 Ma, similar to those of S Naxos (Figure 12). Based on Rb-Sr data most of the ductile deformation had ceased at *c.* 18 Ma (Thomson et al., 2009). Zircon FT ages of  $15.1 \pm 2.4$  Ma (Thomson et al., 2009) indicate cooling below  $\sim 250^\circ\text{C}$  at this time (Figure 12).

### 8.3 | Middle-CBU nappe: Thera island

The samples from Thera correspond to the shallowest part of the Middle-CBU nappe with comparably low-grade peak metamorphic conditions of  $7.6 \pm 1.8$  kbar and  $331 \pm 34^\circ\text{C}$ , as estimated in this study. Peak metamorphism was followed by an overprint at  $\sim 2$  kbar and

$\sim 300^\circ\text{C}$  (Figure 12). Our temperature data are similar to previous estimates (Skarpelis & Liati, 1990), whereas our calculated pressure is  $\sim 4$  kbar lower. Previous work used phengite barometry from an inappropriate paragenesis, which might be an explanation for this deviation. No direct age data constrain the peak of HP metamorphism and the possible lower P-T overprint. Our attempts to date rutile, titanite and apatite were not successful. However,  $^{40}\text{Ar}$ - $^{39}\text{Ar}$  single-grain total fusion data on white mica from metasedimentary samples provide Eocene ages between 54 and 32 Ma for the Middle-CBU nappe (Schneider et al., 2018). Additionally, unpublished U-Pb single-grain zircon data (Lion, 2018) yield apparent age clustering at *c.* 30 Ma (Schneider et al., 2018). Following these data, there is widespread evidence in the Cyclades for Eocene and Oligocene HP metamorphism (see review

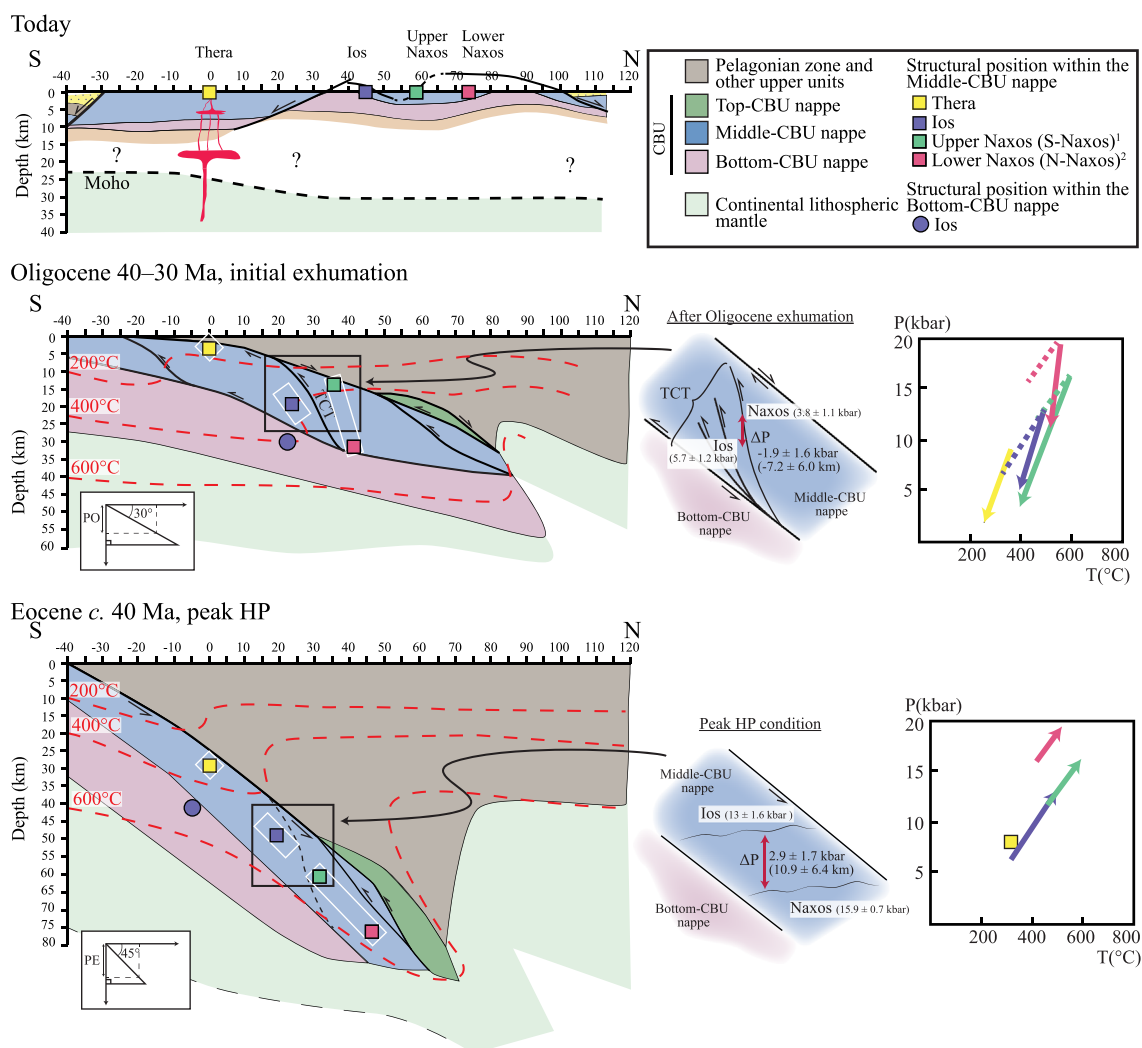


**FIGURE 13** Proposed structural evolution of the middle-CBU nappe for Thera, Ios and Naxos. The inserts on the right show the P-T paths of the selected islands during the Eocene and the Oligocene. The inserts below the tectonic models show a simple geometry sketch of how the horizontal distance between the islands can be calculated from the pressure and a subducting angle. PE: pressure of the island during the Eocene; PO: pressure of the island during the Oligocene. [Colour figure can be viewed at [wileyonlinelibrary.com](http://wileyonlinelibrary.com)]

in Glodny & Ring, 2022). We hence speculate that Thera experienced an Eocene subduction event followed by Oligocene exhumation.

#### 8.4 | Horizontal Eocene and Oligocene distance between the HP units

The original Eocene and Oligocene horizontal distances between the islands of Thera, Ios and Naxos (from south to north) can be calculated using vertical distances (differences in P estimates) and subduction angles at these times. Jolivet and Brun (2010) suggest that the subduction angle decreased from the Eocene until today from 45° to 30°. In the Middle-CBU nappe, between Thera and the lower parts of the-Naxos Middle-CBU nappe a P difference of ~12.3 kbar is observed, corresponding to a vertical distance of ~46 km (assuming an average rock density of 2,700 kg/m<sup>3</sup>). From this vertical distance and an assumed subduction angle of 45°, an original horizontal Eocene distance of 46 km was calculated between Thera and the lower part of Naxos (Table S13). In the Oligocene, the pressure difference between Thera and the lower part of the Middle-CBU nappe on Naxos is ~6.3 kbar, half the P during the Eocene. Assuming that the subduction angle was already close to ~30° in the Oligocene, the horizontal distance decreases to ~41 km, corresponding to ~11% horizontal shortening (Figure 13; Table S13). This shortening apparently mainly affected the region between Ios and Naxos, since the horizontal distance between these two islands decreased from ~26 km to ~17 km whereas the horizontal distance between Thera and Ios remained almost constant at ~22 km.

The Aegean region experienced lithospheric extension during the Miocene due to slab roll back. The exhumation of the CBU during extension resulted in ~72% N-S horizontal crustal stretching for Ios, which is so far the best proxy for the region (Mizera & Behrmann, 2016). Applying this value (72% crustal stretching) to our previous calculations for the distances between the islands after shortening results in values which are close to the ones observed today. (Figure 13; Table S13). For example, the horizontal distance between Thera and the lower part of Middle-CBU of Naxos is calculated at ~74 km which fits with the 80 km measured today (Figure 13; Table S13).

#### 8.5 | Burial and heating rate during subduction of the middle-CBU nappe

Following Glodny and Ring (2022), the Middle-CBU nappe should be regarded as a coherent nappe. Burial,

subduction and heating rates are poorly known. The review of the P-T-t data of the Middle-CBU nappe for Naxos, Ios and Thera presented in this study combined with our new P-T-t data reveal a pressure gradient between these islands with peak P increasing from ~7.5 kbar on Thera, via ~13 kbar on Ios, ~16 kbar near the upper to ~20 kbar in the lowermost part of Middle-CBU nappe. The prograde P-T paths provide thermal gradients of about 6–12°C/km (Figure 14). The slight variations of the thermal gradients of the Middle-CBU Nappe between the islands can be explained by uncertainties in the P and T data, or/and by their structural position within the subducting slab (Peacock, 1993), or/and because the general trend of subduction P-T paths follows a concave upward trajectory from warmer to cooler thermal gradients (Penniston-Dorland et al., 2015). The new U-Pb garnet age data for Ios are key to better understand the Eocene subduction of the Middle-CBU nappe. The age for prograde metamorphism of  $55 \pm 5$  Ma (P-T conditions of  $6.7 \pm 1.4$  kbar,  $326 \pm 20^\circ\text{C}$ ) and for peak HP metamorphism of  $40.1 \pm 1.4$  Ma (P-T conditions of  $13.0 \pm 1.6$  kbar,  $506 \pm 13^\circ\text{C}$ ) allow to calculate Eocene burial and heating rates (Figure 15). The burial rate is  $1.5 \pm 0.6$  km/Ma (Figure 15) which gives a subduction rate of  $2.1 \pm 1.0$  km/Ma assuming a subduction angle of 45° (Jolivet & Brun, 2010). A similar burial rate of  $1.7 \pm 1.4$  km/Ma (subduction rate:  $2.4 \pm 1.9$  km/Ma; Figure 15) is obtained for the upper part of the Middle-CBU nappe of Naxos using the U-Pb zircon ages of Martin et al. (2006) for prograde and peak HP metamorphism (Peillod, Majka, et al., 2021). Such slow subduction rates for the Middle-CBU nappe are typical for continental subduction (Royden & Faccenna, 2018). During this burial, the Middle-CBU nappe of Ios experienced a heating rate of  $12 \pm 4^\circ\text{C}/\text{Ma}$  (Figure 15). The heating rate of  $8 \pm 7^\circ\text{C}/\text{Ma}$  obtained for the Middle-CBU nappe of Naxos overlaps with the one calculated for Ios, however, the uncertainties are rather large. In summary, Thera, Ios and Naxos experienced synchronous prograde and peak HP metamorphism as a coherent nappe (Figure 13).

The subduction rate of ~2.1–2.4 km/Ma obtained in this study for Ios and Naxos can be compared with the one calculated for Sifnos ( $5.9 \pm 1.4$  km/Ma; Dragovic et al., 2015), which is the only other subduction rate available for the Middle-CBU nappe, and with the current subduction rate of ~40–45 km/Ma for the Hellenic subduction zone (Reilinger et al., 2010). The subduction rate calculated from the Ios and Naxos data is slightly lower than the one calculated for Sifnos and both are an order of magnitude lower than the current subduction rate in the Hellenic subduction zone. The slow Eocene subduction rates estimated for Ios, Naxos and Sifnos might reveal a slowdown of the subduction speed when



continental lithosphere is being subducted, as also predicted by numerical modelling (Burov et al., 2014; Royden & Faccenna, 2018).

Numerical models suggest that variations of slow subduction rates can be related to the transition of subduction of a thin, distal to a thick, proximal continental margin (Royden & Faccenna, 2018). Detrital zircon U–Pb data indicate that the western Cyclades, comprising Sifnos, have a distal continental margin affinity whereas Ios has a proximal continental margin affinity (Poulaki et al., 2019; Seman et al., 2017). Based on the original paleogeographic position from the detrital zircon data and the difference in subduction rates estimated between Sifnos ( $5.9 \pm 1.4$  km/Ma) and Ios ( $2.1 \pm 1.0$  km/Ma), the slight slowdown of the subduction rate between islands may be interpreted as reflecting the subduction of the distal and proximal continental margin.

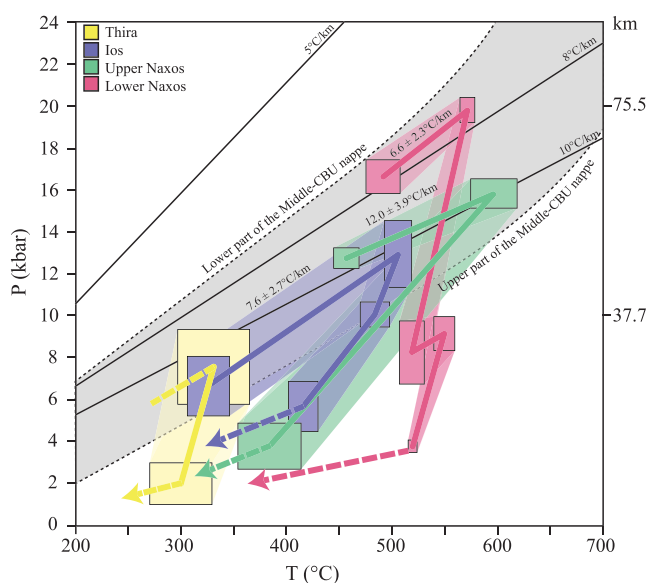


**FIGURE 14** P–T paths of Thera, Ios and Naxos with their P–T trajectories during the subduction. [Colour figure can be viewed at [wileyonlinelibrary.com](http://wileyonlinelibrary.com)]

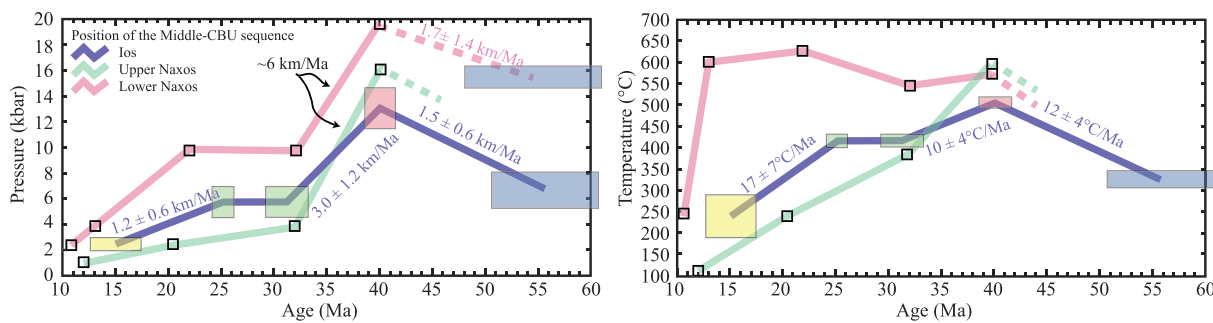


**FIGURE 15** Exhumation (P–t) and cooling (T–t) path for Ios and for Naxos (top and bottom middle-CBU nappe) for comparison. [Colour figure can be viewed at [wileyonlinelibrary.com](http://wileyonlinelibrary.com)]

## 8.6 | Middle- /bottom-CBU nappe contact and internal imbrication of the middle-CBU nappe

The Eocene (c. 40 Ma) peak HP conditions show a P difference of  $\sim 2.9 \pm 1.7$  kbar ( $\Delta P$  in inserts in Figure 13) between the upper parts of the Middle-CBU nappe on Naxos ( $15.9 \pm 0.7$  kbar) and the Middle CBU Nappe on Ios ( $13.0 \pm 1.6$  kbar). Glodny and Ring (2022) propose that the Middle-CBU nappe was exhumed as an extrusion wedge in the early Oligocene after its HP overprint at c. 33–27 Ma. During the Oligocene, the upper Naxos Middle-CBU was exhumed to higher crustal levels ( $3.8 \pm 1.1$  kbar) than the Middle-CBU nappe on Ios ( $5.7 \pm 1.2$  kbar), corresponding to a P difference of  $-1.9 \pm 1.6$  kbar. This indicates that the Naxos section must have been thrust southward onto the Ios Middle CBU Nappe (Figure 13). We think that this thrusting explains the difference in the exhumation rates of Naxos and Ios (6 vs. 3 km/Ma respectively; Figure 15). The P data between Ios and Thera show no P differences between peak HP and the greenschist facies overprint, which indicates that there was no top-to-the-S thrust between these islands causing the burial of the footwall.

Which thrust may have caused the P inversion between Naxos and Ios during exhumation and how was deformation distributed? The Trans Cycladic Thrust (TCT) is the major Oligocene thrust in the Cyclades (Glodny & Ring, 2022). Ring and Glodny (2021) show that the TCT was active during the Oligocene, reimbricated the CBU nappe sequence and also formed the contact between the Bottom- and the Middle-CBU nappes in Sikinos. In other words, the TCT may likely be the Middle- /Bottom-CBU nappe contact. However, based on detrital U–Pb zircon data, Poulaki et al. (2019) propose a series of small-scale thrusts forming km-thick metasediment slices within the Middle-CBU nappe in North Ios. Peillod, Majka, et al. (2021) came to a similar conclusion for Naxos based on a calculated

increase in the crustal thickness of the lower parts of the Middle-CBU nappe during Oligocene exhumation. Collectively, these observations suggest a zone of thrusting at the base of the Middle-CBU nappe in Ios and Naxos. We envisage that the TCT forms the base of the Middle-CBU nappe and thrust splays form a deformation zone associated with the TCT in the lower Middle-CBU nappe. Note that despite the thrusts near the base, the entire Middle-CBU nappe still exhumes as long as displacement(s) at the upper normal(s) fault exceed the thrust displacement(s).

Using the 9–11 kbar estimated by Grütter (1993), the peak pressure of the Bottom-CBU nappe on Ios would be  $3 \pm 1.9$  kbar lower ( $11.3 \pm 7.1$  km; Figures 4 and 13) than that of the Middle-CBU nappe. These estimates suggest a displacement of  $22.7 \pm 18.5$  km at the nappe contact putting the Middle-CBU onto the Bottom-CBU nappe (assuming a  $30^\circ$  thrust dip during the Oligocene).

## 9 | CONCLUSION

We report new P–T paths for the Cycladic islands of Thera and Ios. Our new U–Pb age data for garnet cores and rims of samples from Ios can be directly linked with the P–T values constrained for prograde and peak metamorphism. A review of the existing data for Naxos, Ios and Thera combined with our new data suggests that the studied segments all belong to the Middle-CBU nappe, which acted as one single coherent unit during subduction at a burial rate of  $\sim 1.5$  km/Ma, leading to simultaneous peak HP metamorphism at 42–38 Ma at significantly different peak pressures, depending on their structural position within the subduction slab. During Oligocene exhumation, the lower parts of the Naxos Middle-CBU nappe were thrust over the Middle-CBU nappe on Ios. This indicates that internal deformation and thrust faults developed during the exhumation of the extrusion wedge. The Trans Cycladic Thrust, representing a major regional fault during the Oligocene, is presumably responsible for this imbrication within the Middle-CBU nappe. Synchronously, the Middle-CBU nappe is thrust on the Bottom-CBU nappe on Ios with a displacement of  $\sim 23$  km. Our new findings help to understand the mechanisms of subduction and disruption of a subducted segment of a continental margin during its exhumation.

### AUTHOR CONTRIBUTIONS

Alexandre Peillod is the main writer of the manuscript and revision. He developed the research idea, did field trip sampling, P–T–t review, petrological observations (microscopy and SEM), Zr-in-rutile analyses and data

treatment, RAMAN spectroscopy analyses and data treatment, average P–T calculations, phase equilibrium interpretations, U–Pb garnet age interpretations and all discussion calculations.

Clifford G. C. Patten contributed to project development, field trip sampling, petrological observations and manuscript revision.

Kirsten Drüppel did titration analyses, phase equilibrium calculations and interpretation, contributed to the discussion, part of writing and revising the manuscript.

Aratz Beranoaguirre did U–Pb garnet geochronology analyses and contributed to manuscript writing and revisions.

Armin Zeh did Zr-in-rutile analyses and contributed to manuscript revisions.

Dominik Gudelius provided petrological observation, part of the EPMA analyses and contributed to manuscript revisions.

Simon Hector did field trip sampling and bulk rock analyses and contributed to manuscript revisions.

Jarosław Majka provided support for EPMA analyses and contributed to the manuscript revisions.

Barbara I. Kleine-Marshall contributed to field trip sampling and manuscript revisions.

Andreas Karlson provided support for SEM imaging.

Axel Gerdes provided support for U–Pb garnet geochronology.

Jochen Kolb contributed to manuscript revisions.

### ACKNOWLEDGMENTS

This paper is dedicated to my late father, Maurice Peillod. The work has received funding from the German Research Foundation (DFG; project numbers 02020830221 and INST121384/213-1 FUGG) and from the Bolin Centre for Climate Research (RA6\_19\_09\_Peillod). We are thankful for the reviews by Eirini Poulaki and Michael Bröcker, which helped us to improve the manuscript as well as for the editorial handling by Sarah Penniston-Dorland. Deep thanks as well to Uwe Ring and Igor Villa for the useful comments.

### DATA AVAILABILITY STATEMENT

The data that supports the findings of this study are available in the supplementary material of this article.

### ORCID

Alexandre Peillod  <https://orcid.org/0000-0001-6378-6918>

Aratz Beranoaguirre  <https://orcid.org/0000-0002-1137-6498>

Jarosław Majka  <https://orcid.org/0000-0002-6792-6866>

Andreas Karlson  <https://orcid.org/0000-0002-5390-0577>

## REFERENCES

- Andriessen, P. A. M. (1978). *Isotopic age relations within the polymetamorphic complex of the island of Naxos*. Cyclades.
- Andriessen, P. A. M., Boelrijk, N. A. I. M., Hebeda, E. H., Priem, H. N. A., Verdurnen, E. A. T., & Verschure, R. H. (1979). Dating the events of metamorphism and granitic magmatism in the Alpine orogen of Naxos (Cyclades, Greece). *Contributions to Mineralogy and Petrology*, *69*, 215–225. <https://doi.org/10.1007/BF00372323>
- Angiboust, S., & Harlov, D. (2017). Ilmenite breakdown and rutile-titanite stability in metagranitoids: Natural observations and experimental results. *American Mineralogist*, *102*, 1696–1708. <https://doi.org/10.2138/am-2017-6064>
- Aravadinou, E., & Xypolias, P. (2017). Evolution of a passive crustal-scale detachment (Syros, Aegean region): Insights from structural and petrofabric analyses in the hanging-wall. *Journal of Structural Geology*, *103*, 57–74. <https://doi.org/10.1016/j.jsg.2017.09.008>
- Avigad, D. (1998). High-pressure metamorphism and cooling on SE Naxos (Cyclades, Greece). *European Journal of Mineralogy*, *10*, 1309–1320. <https://doi.org/10.1127/ejm/10/6/1309>
- Avigad, D., & Garfunkel, Z. (1991). Uplift and exhumation of high-pressure metamorphic terrains: The example of the cycladic blueschist belt (Aegean Sea). *Tectonophysics*, *188*, 357–372. [https://doi.org/10.1016/0040-1951\(91\)90464-4](https://doi.org/10.1016/0040-1951(91)90464-4)
- Baldwin, S. L. (1996). Contrasting P-T-t histories for blueschists from the western Baja terrane and the aegean: Effects of synsubduction exhumation and backarc extension. *Geophysical Monograph Series*, *96*, 135–141. <https://doi.org/10.1029/GM096p0135>
- Baldwin, S. L., & Lister, S. (1998). Thermochronology of the South Cyclades shear zone, Ios, Greece: Effects of ductile shear in the argon partial retention zone. *Journal of Geophysical Research*, *103*, 7315–7336. <https://doi.org/10.1029/97JB03106>
- Beaudoin, A., Augier, R., Laurent, V., Jolivet, L., Lahfid, A., Bosse, V., Arbaret, L., Rabillard, A., & Menant, A. (2015). The Ikaria high-temperature metamorphic core complex (Cyclades, Greece): Geometry, kinematics and thermal structure. *Journal of Geodynamics*, *92*, 18–41. <https://doi.org/10.1016/j.jog.2015.09.004>
- Bolhar, R., Ring, U., & Ireland, T. R. (2017). Zircon in amphibolites from Naxos, Aegean Sea, Greece: Origin, significance and tectonic setting. *Journal of Metamorphic Geology*, *35*, 413–434. <https://doi.org/10.1111/jmg.12238>
- Brichau, S., Ring, U., Ketcham, R. A., Carter, A., Stockli, D., & Brunel, M. (2006). Constraining the long-term evolution of the slip rate for a major extensional fault system in the Central Aegean, Greece, using thermochronology. *Earth and Planetary Science Letters*, *241*, 293–306. <https://doi.org/10.1016/j.epsl.2005.09.065>
- Bröcker, M., Baldwin, S., & Arkudas, R. (2013). The geological significance of  $^{40}\text{Ar}/^{39}\text{Ar}$  and Rb-Sr white mica ages from Syros and Sifnos, Greece: A record of continuous (re)crystallization during exhumation? *Journal of Metamorphic Geology*, *31*, 629–646. <https://doi.org/10.1111/jmg.12037>
- Buick, I. S. (1991). Mylonite fabric development on Naxos, Greece. *Journal of Structural Geology*, *13*, 643–655. [https://doi.org/10.1016/0191-8141\(91\)90027-G](https://doi.org/10.1016/0191-8141(91)90027-G)
- Buick, I. S., & Holland, T. J. B. (1989). The P-T-t path associated with crustal extension, Naxos, Cyclades, Greece. *Geological Society of London, Special Publication*, *1*, 365–369. <https://doi.org/10.1144/GSL.SP.1989.043.01.32>
- Burov, E., Francois, T., Yamato, P., & Wolf, S. (2014). Mechanisms of continental subduction and exhumation of HP and UHP rocks. *Gondwana Research*, *25*, 464–493. <https://doi.org/10.1016/j.gr.2012.09.010>
- Cao, S., Neubauer, F., Bernroider, M., & Genser, J. (2018). Eocene high-pressure metamorphism and Oligocene retrogression on Naxos, Cyclades, Greece: Significance for Aegean tectonics and  $^{40}\text{Ar}/^{39}\text{Ar}$  dating in polyphase metamorphic rocks. *Tectonophysics*, *745*, 66–94. <https://doi.org/10.1016/j.tecto.2018.08.009>
- Cao, S., Neubauer, F., Bernroider, M., Genser, J., Liu, J., & Friedl, G. (2017). Low-grade retrogression of a high-temperature metamorphic core complex: Naxos, Cyclades, Greece. *Bulletin Geological Society of America*, *129*, 93–117. <https://doi.org/10.1130/B31502.1>
- Dragovic, B., Baxter, E. F., & Caddick, M. J. (2015). Pulsed dehydration and garnet growth during subduction revealed by zoned garnet geochronology and thermodynamic modeling, Sifnos, Greece. *Earth and Planetary Science Letters*, *413*, 111–122. <https://doi.org/10.1016/j.epsl.2014.12.024>
- Ducharme, T. A., Schneider, D. A., Grasemann, B., & Klonowska, I. (2022). Stretched thin: Oligocene extrusion and ductile thinning of the basal unit along the Evia shear zone, NW Cyclades. *Tectonics*, *41*(12), e2022TC007561. <https://doi.org/10.1029/2022TC007561>
- Duchêne, S., Aïssa, R., & Vanderhaeghe, O. (2006). Pressure-temperature-time evolution of metamorphic rocks from Naxos (Cyclades, Greece): Constraints from thermobarometry and Rb/Sr dating. *Geodinamica Acta*, *19*, 299–319. <https://doi.org/10.3166/ga.19.301-321>
- Dürr, S. (1978). The median Aegean crystalline belt stratigraphy, structure, metamorphism, magnetism. In *Alps, Apennines, Hellenides* (pp. 455–477).
- Ernst, W. G. (2001). Subduction, ultrahigh-pressure metamorphism, and regurgitation of buoyant crustal slices—Implications for arcs and continental growth. *Physics of the Earth and Planetary Interiors*, *127*, 253–275. [https://doi.org/10.1016/S0031-9201\(01\)00231-X](https://doi.org/10.1016/S0031-9201(01)00231-X)
- Ernst, W. G., Maruyama, S., & Wallis, S. (1997). Buoyancy-driven, rapid exhumation of ultrahigh-pressure metamorphosed continental crust. *Proceedings of the National Academy of Sciences of the United States of America*, *94*, 9532–9537. <https://doi.org/10.1073/pnas.94.18.9532>
- Feenstra, A. (1985). Metamorphism of bauxites on Naxos, Greece. Dr. Diss. Inst. voor Aardwetenschappen RUU.
- Flansburg, M. E., Poulaki, E. M., Stockli, D. F., & Soukis, K. (2022). Coeval Miocene exhumation of the Cycladic Blueschist unit and the Cycladic basement in the southern Cyclades, Ios and Sifnos, Greece. *Terra Nova*, *35*, 124–133. <https://doi.org/10.1111/ter.12636>
- Flansburg, M. E., Stockli, D. F., Poulaki, E. M., & Soukis, K. (2019). Tectono-magmatic and stratigraphic evolution of the cycladic basement, Ios Island, Greece. *Tectonics*, *38*, 2291–2316. <https://doi.org/10.1029/2018TC005436>
- Forster, M., Koudashev, O., Nie, R., Yeung, S., & Lister, G. (2020).  $^{40}\text{Ar}/^{39}\text{Ar}$  thermochronology in the Ios basement terrane resolves the tectonic significance of the South Cyclades shear

- zone. *Geological Society - Special Publications*, 487, 291–313. <https://doi.org/10.1144/SP487-2018-169>
- Forster, M., & Lister, G. (2009). Core-complex-related extension of the Aegean lithosphere initiated at the Eocene-Oligocene transition. *Journal of Geophysical Research - Solid Earth*, 114, B02401. <https://doi.org/10.1029/2007JB005382>
- Forster, M. A., & Lister, G. S. (1999a). Separate episodes of eclogite and blueschist facies metamorphism in the Aegean metamorphic core complex of Ios, Cyclades, Greece. *Geological Society - Special Publications*, 164, 157–177. <https://doi.org/10.1144/GSL.SP.1999.164.01.09>
- Forster, M. A., & Lister, G. S. (1999b). Detachment faults in the Aegean core complex of Ios, Cyclades, Greece. *Geological Society - Special Publications*, 154, 305–323. <https://doi.org/10.1144/GSL.SP.1999.154.01.14>
- Gautier, P., Brun, J. P., & Jolivet, L. (1993). Structure and kinematics of upper Cenozoic extensional detachment on Naxos and Paros (Cyclades Island, Greece). *Tectonics*, 12, 1180–1194. <https://doi.org/10.1029/93TC01131>
- Gerya, T. V., Stöckhert, B., & Perchuk, A. L. (2002). Exhumation of high-pressure metamorphic rocks in a subduction channel: A numerical simulation. *Tectonics*, 21, 6–1–6–19. <https://doi.org/10.1029/2002tc001406>
- Gessner, K., Ring, U., Passchier, C. W., & Güngör, T. (2001). How to resist subduction: Evidence for large-scale out-of-sequence thrusting during Eocene collision in Western Turkey. *Journal of the Geological Society of London*, 158, 769–784. <https://doi.org/10.1144/jgs.158.5.769>
- Glodny, J., & Ring, U. (2022). The Cycladic Blueschist unit of the Hellenic subduction orogen: Protracted high-pressure metamorphism, decompression and reimbrication of a diachronous nappe stack. *Earth-Science Reviews*, 224, 103883. <https://doi.org/10.1016/j.earscirev.2021.103883>
- Gorce, J. S., Caddick, M. J., Baxter, E. F., Dragovic, B., Schumacher, J. C., Bodnar, R. J., & Kendall, J. F. (2021). Insight into the early exhumation of the Cycladic Blueschist unit, Syros, Greece: Combined application of zoned garnet geochronology, thermodynamic modeling, and quartz elastic barometry. *Geochemistry, Geophysics, Geosystems*, 22, 1–24. <https://doi.org/10.1029/2021GC009716>
- Grasemann, B., Huet, B., Schneider, D. A., Rice, A. H. N., Lemonnier, N., & Tschegg, C. (2018). Miocene postorogenic extension of the Eocene synorogenic imbricated Hellenic subduction channel: New constraints from Milos (Cyclades, Greece). *Bulletin Geological Society of America*, 130, 238–262. <https://doi.org/10.1130/B31731.1>
- Grütter, H. S. (1993). Structural and metamorphic studies on Ios, Cyclades, Greece 279.
- Guillot, S., Hattori, K., Agard, P., Schwartz, S., & Vidal, O. (2009). Exhumation processes in oceanic and continental subduction contexts: A review. [https://doi.org/10.1007/978-3-540-87974-9\\_10](https://doi.org/10.1007/978-3-540-87974-9_10)
- Hejl, E., de Grave, J., Riedl, H., Weingartner, H., & van den Haute, P. (2008). Fission-track thermochronology of the middle Aegean Island bridge—Implications for Neogene geomorphology and palaeogeography. *Zeitschrift der Dtsch. Gesellschaft Fur Geowissenschaften*, 159, 495–512. <https://doi.org/10.1127/1860-1804/2008/0159-0495>
- Hejl, E., Riedl, H., Soulakellis, N., Van den Haute, P., & Weingartner, H. (2003). Young Neogene tectonics and relief development on the Aegean Islands of Naxos, Paros and Ios (Cyclades, Greece). *Mitteilungen der Österreichischen Geographischen Gesellschaft*, 93, 105–127.
- Henjes-Kunst, F., & Kreuzer, H. (1982). Isotopic dating of pre-Alpidic rocks from the island of Ios (Cyclades, Greece). *Contributions to Mineralogy and Petrology*, 80, 245–253. <https://doi.org/10.1007/BF00371354>
- van Hinsbergen, D. J. J., Hafkenscheid, E., Spakman, W., Meulenkamp, J. E., & Wortel, R. (2005). Nappe stacking resulting from subduction of oceanic and continental lithosphere below Greece. *Geology*, 33, 325–328. <https://doi.org/10.1130/G20878.1>
- Huet, B. (2010). Rhéologie de la lithosphère continentale: L'exemple de la Mer Egée. Doctoral dissertation, Université Pierre et Marie Curie-Paris VI.
- Huet, B., Labrousse, L., & Jolivet, L. (2009). Thrust or detachment? Exhumation processes in the Aegean: Insight from a field study on Ios (Cyclades, Greece). *Tectonics*, 28, 1–27. <https://doi.org/10.1029/2008TC002397>
- Jansen, J. B. H., & Schuiling, R. D. (1976). Metamorphism on Naxos; petrology and geothermal gradients. *American Journal of Science*, 276, 1225–1253. <https://doi.org/10.2475/ajs.276.10.1225>
- Jolivet, L., & Brun, J. P. (2010). Cenozoic geodynamic evolution of the Aegean. *International Journal of Earth Sciences*, 99, 109–138. <https://doi.org/10.1007/s00531-008-0366-4>
- Jolivet, L., Lecomte, E., Huet, B., Denèle, Y., Lacombe, O., Labrousse, L., Le Pourhiet, L., & Mehl, C. (2010). The north Cycladic detachment system. *Earth and Planetary Science Letters*, 289, 87–104. <https://doi.org/10.1016/j.epsl.2009.10.032>
- Jolivet, L., Sautter, V., Moretti, I., Vettor, T., Papadopoulou, Z., Augier, R., Denèle, Y., & Arbaret, L. (2021). Anatomy and evolution of a migmatite-cored extensional metamorphic dome and interaction with syn-kinematic intrusions, the Mykonos-Delos-Rheneia MCC. *Journal of Geodynamics*, 144, 101824. <https://doi.org/10.1016/j.jog.2021.101824>
- Jones, G., & Robertson, A. H. F. (1991). Tectono-stratigraphy and evolution of the Mesozoic Pindos ophiolite and related units, northwestern Greece. *Journal of the Geological Society of London*, 148, 267–288. <https://doi.org/10.1144/gsjgs.148.2.0267>
- Keay, S., Lister, G., & Buick, I. (2001). The timing of partial melting, Barrovian metamorphism and granite intrusion in the Naxos metamorphic core complex, Cyclades, Aegean Sea, Greece. *Tectonophysics*, 342, 275–312. [https://doi.org/10.1016/S0040-1951\(01\)00168-8](https://doi.org/10.1016/S0040-1951(01)00168-8)
- Kilias, A., Frisch, W., Avgerinas, A., Dunkl, I., Falalakis, G., & Al, E. (2010). The Pelagonian nappe pile in northern Greece and Fyrom. Structural evolution during the Alpine orogeny: A new approach. *Bulletin of the Geological Society of Greece*, 43, 276. <https://doi.org/10.12681/bgsg.11180>
- Kotowski, A. J., Cisneros, M., Behr, W. M., Stockli, D. F., Soukis, K., Barnes, J. D., & Ortega-Arroyo, D. (2022). Subduction, underplating, and return flow recorded in the Cycladic Blueschist unit exposed on Syros, Greece. *Tectonics*, 41(6), e2020TC006528. <https://doi.org/10.1029/2020tc006528>
- Kreuzer, H., Harre, W., Lenz, H., Wendt, I., & Henjes-Kunst, F. (1978). K/Ar- und Rb/Sr- Daten von Mineralen aus dem

- polymetamorphen Kristallin der Kykladen-Insel Ios (Griechenland). *Fortschritte der Mineralogie*, 56, 69–70.
- Kruckenbergh, S. C., Ferré, E. C., Teyssier, C., Vanderhaeghe, O., Whitney, D. L., Seaton, N. C. A., & Skord, J. A. (2010). Viscoplastic flow in migmatites deduced from fabric anisotropy: An example from the Naxos dome, Greece. *Journal of Geophysical Research: Solid Earth*, 115, 1–18. <https://doi.org/10.1029/2009JB007012>
- Kuhlemann, J., Frisch, W., Dunkl, I., Kázmér, M., & Schmiedl, G. (2004). Miocene siliciclastic deposits of Naxos Island: Geodynamic and environmental implications for the evolution of the southern Aegean Sea (Greece). *Special Paper of the Geological Society of America*, 378, 51–65. <https://doi.org/10.1130/0-8137-2378-7.51>
- Kumerics, C., Ring, U., Brichau, S., Glodny, J., & Monié, P. (2005). The extensional Messaria shear zone and associated brittle detachment faults, Aegean Sea, Greece. *Journal of the Geological Society*, 162, 701–721. <https://doi.org/10.1144/0016-764904-041>
- Lamont, T. N., Searle, M. P., Waters, D. J., Roberts, N. M. W., Palin, R. M., Smye, A., Dyck, B., Gopon, P., Weller, O. M., & St-onge, M. R. (2019). Compressional origin of the Naxos metamorphic core complex, Greece: Structure, petrography, and thermobarometry. *Geological Society of America Bulletin*, 1–49, 149–197. <https://doi.org/10.1130/B31978.1/4719075/b31978.pdf>
- Lamont, T. N., Smye, A. J., Roberts, N. M. W., Searle, M. P., Waters, D. J., & White, R. W. (2023). Constraints on the thermal evolution of metamorphic core complexes from the timing of high-pressure metamorphism on Naxos, Greece. *Geological Society of America Bulletin*, 135(11–12), 2767–2796. <https://doi.org/10.1130/B36332.1>
- Laurent, V., Huet, B., Labrousse, L., Jolivet, L., Monié, P., & Augier, R. (2017). Extraneous argon in high-pressure metamorphic rocks: Distribution, origin and transport in the Cycladic Blueschist unit (Greece). *Lithos*, 272–273, 315–335. <https://doi.org/10.1016/j.lithos.2016.12.013>
- Lion, A. (2018). *Thermochronologic and geochronologic investigations of the pre-volcanic crystalline basement of Thera (Santorini), Greece: Determining the tectonostratigraphy and deformational history of the metamorphic core*. University of Ottawa.
- Lister, G. S., & Forster, M.A. (1996). Inside the Aegean Metamorphic Core Complexes: A Field Trip Guide Illustrating the Geology of 27, 41–46. <https://doi.org/10.3809/doi>
- Lister, G. S., & Forster, M. A. (2016). White mica  $^{40}\text{Ar}/^{39}\text{Ar}$  age spectra and the timing of multiple episodes of high-P metamorphic mineral growth in the Cycladic eclogite-blueschist belt, Syros, Aegean Sea, Greece. *Journal of Metamorphic Geology*, 34, 401–421. <https://doi.org/10.1111/jmg.12178>
- van der Maar, P. A., & Jansen, J. B. H. (1983). The geology of the polymetamorphic complex of Ios, Cyclades, Greece and its significance for the Cycladic massif. *Geologische Rundschau*, 72, 283–299. <https://doi.org/10.1007/BF01765910>
- Mancktelow, N., Zwingmann, H., & Mulch, A. (2016). Timing and conditions of clay fault gouge formation on the Naxos detachment (Cyclades, Greece). *Tectonics*, 35, 2334–2344. <https://doi.org/10.1002/2016TC004251>
- Martin, L. (2004). *Signification des âges U-Pb Sur zircon dans l'histoire métamorphique de Naxos et Ikaria (Cyclades, Grèce)*. Université Henri Poincaré.
- Martin, L., Duchêne, S., Deloule, E., & Vanderhaeghe, O. (2006). The isotopic composition of zircon and garnet: A record of the metamorphic history of Naxos, Greece. *Lithos*, 87, 174–192. <https://doi.org/10.1016/j.lithos.2005.06.016>
- Mizera, M., & Behrmann, J. H. (2016). Strain and flow in the metamorphic core complex of Ios Island (Cyclades, Greece). *International Journal of Earth Sciences*, 105, 2097–2110. <https://doi.org/10.1007/s00531-015-1259-y>
- Morimoto, N., Fabries, J., Ferguson, A. K., Ginzburg, I. V., Ross, M., Seifert, F. A., Zussman, J., Aoki, K., & Gottardi, G. (1988). Nomenclature of pyroxenes. *Mineralogical Magazine*, 52, 535–550. <https://doi.org/10.1180/minmag.1988.052.367.15>
- Okay, A. I. (1980). Sodic amphiboles as oxygen fugacity indicators in metamorphism. *Journal of Geology*, 88, 225–232. <https://doi.org/10.1086/628493>
- Okrusch, M., & Bröcker, M. (1990). Eclogites associated with high-grade blueschists in the Cyclades archipelago, Greece: A review. *European Journal of Mineralogy*, 2, 451–478. <https://doi.org/10.1127/ejm/2/4/0451>
- Papanikolaou, D. (2013). Tectonostratigraphic models of the Alpine terranes and subduction history of the Hellenides. *Tectonophysics*, 595–596, 1–24. <https://doi.org/10.1016/j.tecto.2012.08.008>
- Peacock, S. M. (1993). The importance of blueschist → eclogite dehydration reactions in subducting oceanic crust. *Geological Society of America Bulletin*, 105, 684–694. [https://doi.org/10.1130/0016-7606\(1993\)105<0684:TIOBED>2.3.CO;2](https://doi.org/10.1130/0016-7606(1993)105<0684:TIOBED>2.3.CO;2)
- Peillod, A. (2018). *The metamorphic history of Naxos (Central Cyclades, Greece): Deciphering the Oligocene and Miocene exhumation events*. Stockholm University.
- Peillod, A., Majka, J., Ring, U., Drüppel, K., Patten, C., Karlsson, A., Włodek, A., & Tehler, E. (2021). Differences in decompression of a high-pressure unit: A case study from the Cycladic Blueschist unit on Naxos Island, Greece. *Lithos*, 386–387, 106043. <https://doi.org/10.1016/j.lithos.2021.106043>
- Peillod, A., Ring, U., Glodny, J., & Skelton, A. (2017). An Eocene/Oligocene blueschist–greenschist facies P–T loop from the Cycladic Blueschist unit on Naxos Island, Greece: Deformation-related re-equilibration vs. thermal relaxation. *Journal of Metamorphic Geology*, 35, 805–830. <https://doi.org/10.1111/jmg.12256>
- Peillod, A., Tehler, E., & Ring, U. (2021). Quo vadis Zeus: Is there a Zas shear zone on Naxos Island, Aegean Sea, Greece? A review of metamorphic history and new kinematic data. *Journal of the Geological Society of London*, 178, jgs2020-217. <https://doi.org/10.1144/jgs2020-217>
- Penniston-Dorland, S. C., Kohn, M. J., & Manning, C. E. (2015). The global range of subduction zone thermal structures from exhumed blueschists and eclogites: Rocks are hotter than models. *Earth and Planetary Science Letters*, 428, 243–254. <https://doi.org/10.1016/j.epsl.2015.07.031>
- Platt, J. P. (1993). Exhumation of high-pressure rocks: A review of concepts and processes. *Terra Nova*, 5, 119–133. <https://doi.org/10.1111/j.1365-3121.1993.tb00237.x>
- Poulaki, E. M., Stockli, D. F., Flansburg, M. E., Gevedon, M. L., Stockli, L. D., Barnes, J. D., Soukiss, K., Kitajima, K., & Valley, J. W. (2021). Zircon U–Pb and geochemical signatures

- in high-pressure, low-temperature metamorphic rocks as recorders of subduction zone processes, Sikinos and Ios islands, Greece. *Chemical Geology*, 582, 120447. <https://doi.org/10.1016/j.chemgeo.2021.120447>
- Poulaki, E. M., Stockli, D. F., Flansburg, M. E., & Soukis, K. (2019). Zircon U-Pb chronostratigraphy and provenance of the Cycladic Blueschist unit and the nature of the contact with the Cycladic basement on Sikinos and Ios Islands, Greece. *Tectonics*, 38, 3586–3613. <https://doi.org/10.1029/2018TC005403>
- Reilinger, R., McClusky, S., Paradissis, D., Ergintav, S., & Vernant, P. (2010). Geodetic constraints on the tectonic evolution of the Aegean region and strain accumulation along the Hellenic subduction zone. *Tectonophysics*, 488, 22–30. <https://doi.org/10.1016/j.tecto.2009.05.027>
- Ring, U., & Glodny, J. (2010). No need for lithospheric extension for exhuming (U)HP rocks by normal faulting. *Journal of the Geological Society of London*, 167, 225–228. <https://doi.org/10.1144/0016-76492009-134>
- Ring, U., & Glodny, J. (2021). Geometry and kinematics of bivergent extension in the southern Cycladic archipelago: Constraining an extensional hinge zone on Sikinos Island, Aegean Sea, Greece. *Tectonics*, 40, 1–24. <https://doi.org/10.1029/2020TC006641>
- Ring, U., Glodny, J., Peillod, A., & Skelton, A. (2018). The timing of high-temperature conditions and ductile shearing in the footwall of the Naxos extensional fault system, Aegean Sea, Greece. *Tectonophysics*, 745, 366–381. <https://doi.org/10.1016/j.tecto.2018.09.001>
- Ring, U., Glodny, J., Will, T., & Thomson, S. (2007). An Oligocene extrusion wedge of blueschist-facies nappes on Evia, Aegean Sea, Greece: Implications for the early exhumation of high-pressure rocks. *Journal of the Geological Society of London*, 164, 637–652. <https://doi.org/10.1144/0016-76492006-041>
- Ring, U., Glodny, J., Will, T., & Thomson, S. (2010). The Hellenic subduction system: High-pressure metamorphism, exhumation, normal faulting, and large-scale extension. *Annual Review of Earth and Planetary Sciences*, 38, 45–76. <https://doi.org/10.1146/annurev.earth.050708.170910>
- Ring, U., Laws, S., & Bernet, M. (1999). Structural analysis of a complex nappe sequence and late-orogenic basins from the Aegean Island of Samos, Greece. *Journal of Structural Geology*, 21, 1575–1601. [https://doi.org/10.1016/S0191-8141\(99\)00108-X](https://doi.org/10.1016/S0191-8141(99)00108-X)
- Ring, U., & Layer, P. W. (2003). High-pressure metamorphism in the Aegean, eastern Mediterranean: Underplating and exhumation from the late Cretaceous until the Miocene to recent above the retreating Hellenic subduction zone. *Tectonics*, 22, 6–1. <https://doi.org/10.1029/2001TC001350>
- Ring, U., Pantazides, H., Glodny, J., & Skelton, A. (2020). Forced return flow deep in the subduction channel, Syros, Greece. *Tectonics*, 39(1), e2019TC005768. <https://doi.org/10.1029/2019TC005768>
- Ring, U., Thomson, S. N., & Bröcker, M. (2003). Fast extension but little exhumation: The Vari detachment in the Cyclades, Greece. *Geological Magazine*, 140, 245–252. <https://doi.org/10.1017/S0016756803007799>
- Ring, U., Will, T., Glodny, J., Kumerics, C., Gessner, K., Thomson, S., Güngör, T., Monié, P., Okrusch, M., & Drüppel, K. (2007). Early exhumation of high-pressure rocks in extrusion wedges: Cycladic blueschist unit in the eastern Aegean, Greece, and Turkey. *Tectonics*, 26, 1–23. <https://doi.org/10.1029/2005TC001872>
- Royden, L., & Faccenna, C. (2018). Subduction orogeny and the late Cenozoic evolution of the Mediterranean arcs. *Annual Review of Earth and Planetary Sciences*, 46, 261–289. <https://doi.org/10.1146/annurev-earth-060115-012419>
- Schmid, S. M., Fügenschuh, B., Kounov, A., Mañenco, L., Nievergelt, P., Oberhänsli, R., Pleuger, J., Schefer, S., Schuster, R., Tomljenović, B., Ustaszewski, K., & van Hinsbergen, D. J. J. (2020). Tectonic units of the Alpine collision zone between eastern Alps and western Turkey. *Gondwana Research*, 78, 308–374. <https://doi.org/10.1016/j.gr.2019.07.005>
- Schneider, D. A., Grasemann, B., Lion, A., Soukis, K., & Draganits, E. (2018). Geodynamic significance of the Santorini detachment system (Cyclades, Greece). *Terra Nova*, 30, 414–422. <https://doi.org/10.1111/ter.12357>
- Seman, S., Stockli, D. F., & Soukis, K. (2017). The provenance and internal structure of the Cycladic Blueschist unit revealed by detrital zircon geochronology, Western Cyclades, Greece. *Tectonics*, 36, 1407–1429. <https://doi.org/10.1002/2016TC004378>
- Seward, D., Vanderhaeghe, O., Siebenaller, L., Thomson, S., Hibsich, C., Zingg, A., Holzner, P., Ring, U., & Duchêne, S. (2009). Cenozoic tectonic evolution of Naxos Island through a multi-faceted approach of fission-track analysis. *Geological Society - Special Publications*, 321, 179–196. <https://doi.org/10.1144/SP321.9>
- Skarpelis, N., & Liati, A. (1990). The prevolcanic basement of Thera at Athinios: Metamorphism, Plutonism and Mineralization. In D. Hardy (Ed.), *Proc. Third Int. Congr. "Thera Aegean World."* (pp. 172–182). Thera Found.
- Skelton, A., Peillod, A., Glodny, J., Klonowska, I., Månbro, C., Lodin, K., & Ring, U. (2019). Preservation of high-P rocks coupled to rock composition and the absence of metamorphic fluids. *Journal of Metamorphic Geology*, 37, 359–381. <https://doi.org/10.1111/jmg.12466>
- Thomson, S. N., Ring, U., Brichau, S., Glodny, J., & Will, T. M. (2009). Timing and nature of formation of the Ios metamorphic core complex, southern Cyclades, Greece. *Geological Society - Special Publications*, 321, 139–167. <https://doi.org/10.1144/SP321.7>
- Tual, L., Smit, M. A., Cutts, J., Kooijman, E., Kielman-Schmitt, M., Majka, J., & Foulds, I. (2022). Rapid, paced metamorphism of blueschists (Syros, Greece) from laser-based zoned Lu-Hf garnet chronology and LA-ICPMS trace element mapping. *Chemical Geology*, 607, 121003. <https://doi.org/10.1016/j.chemgeo.2022.121003>
- Uunk, B., Brouwer, F., de Paz-Álvarez, M., van Zuilen, K., Huybens, R., van't Veer, R., & Wijbrans, J. (2022). Consistent detachment of supracrustal rocks from a fixed subduction depth in the Cyclades. *Earth and Planetary Science Letters*, 584, 117479. <https://doi.org/10.1016/j.epsl.2022.117479>
- Vandenberg, L. C., & Lister, G. S. (1996). Structural analysis of basement tectonites from the Aegean metamorphic core complex of Ios, Cyclades, Greece. *Journal of Structural Geology*, 18, 1437–1454. [https://doi.org/10.1016/S0191-8141\(96\)00068-5](https://doi.org/10.1016/S0191-8141(96)00068-5)

- Vanderhaeghe, O. (2004). Structural development of the Naxos migmatite dome. *Special Paper of the Geological Society of America*, 380, 211–227. <https://doi.org/10.1130/0-8137-2380-9.211>
- Vanderhaeghe, O., Kruckenberg, S. C., Gerbault, M., Martin, L., Duchêne, S., & Deloule, E. (2018). Crustal-scale convection and diapiric upwelling of a partially molten orogenic root (Naxos dome, Greece). *Tectonophysics*, 746, 459–469. <https://doi.org/10.1016/j.tecto.2018.03.007>
- Villa, I. M., Glodny, J., Peillod, A., Skelton, A., & Ring, U. (2022). Petrochronology of polygenetic white micas (Naxos, Greece). *Journal of Metamorphic Geology*, 1–23, 401–423. <https://doi.org/10.1111/jmg.12700>
- Warren, C. J., Hanke, F., & Kelley, S. P. (2012). When can muscovite  $^{40}\text{Ar}/^{39}\text{Ar}$  dating constrain the timing of metamorphic exhumation? *Chemical Geology*, 291, 79–86. <https://doi.org/10.1016/j.chemgeo.2011.09.017>
- Whitney, D. L., & Evans, B. W. (2010). Abbreviations for names of rock-forming minerals. *American Mineralogist*, 95, 185–187. <https://doi.org/10.2138/am.2010.3371>
- Wijbrans, J. R., & McDougall, I. (1986).  $^{40}\text{Ar}/^{39}\text{Ar}$  dating of white micas from an Alpine high-pressure metamorphic belt on Naxos (Greece): The resetting of the argon isotopic system. *Contributions to Mineralogy and Petrology*, 93, 187–194. <https://doi.org/10.1007/BF00371320>
- Wijbrans, J. R., & McDougall, I. (1988). Metamorphic evolution of the attic Cycladic Metamorphic Belt. *Journal of Metamorphic Geology*, 6, 571–594. <https://doi.org/10.1111/j.1525-1314.1988.tb00441.x>

## SUPPORTING INFORMATION

Additional supporting information can be found online in the Supporting Information section at the end of this article.

**Supplementary information S1.** Methods.

**Supplementary information S2.** Coordinates and a short sample description.

**Supplementary information S3.** Paragenetic sequences.

**Figure S1 to S6.** Additional petrological observations.

**Figure S7.** Thermodynamic model and discussion.

**Table S1.** Representative garnet analyses.

**Table S2.** Representative pyroxene analyses.

**Table S3.** Representative amphibole analyses.

**Table S4.** Representative epidote analyses.

**Table S5.** Representative feldspar analyses.

**Table S6.** Representative chlorite analyses.

**Table S7.** Representative calcite analyses.

**Table S8.** Representative white mica analyses.

**Table S9.** Representative pumpellyite analyses.

**Table S10.** Representative rutile analyses.

**Table S11.** Representative Raman quartz data.

**Table S12.** LA-ICP-MS U-Th-Pb data report.

**Table S13.** Relative horizontal distance between island.

**How to cite this article:** Peillod, A., Patten, C. G. C., Drüppel, K., Beranoaguirre, A., Zeh, A., Gudelius, D., Hector, S., Majka, J., Kleine-Marshall, B. I., Karlson, A., Gerdes, A., & Kolb, J. (2023). Disruption of a high-pressure unit during exhumation: Example of the Cycladic Blueschist unit (Thera, Ios and Naxos islands, Greece). *Journal of Metamorphic Geology*, 1–31. <https://doi.org/10.1111/jmg.12753>